

## Article

# Synthesis of *n*-Alkoxy Derivatives of Layered Perovskite-Like Niobate $\text{HCa}_2\text{Nb}_3\text{O}_{10}$ and Study of Their Photocatalytic Activity for Hydrogen Production from an Aqueous Solution of Methanol

Vladimir V. Voytovich <sup>1</sup>, Sergey A. Kurnosenko <sup>1</sup>, Oleg I. Silyukov <sup>1,\*</sup>, Ivan A. Rodionov <sup>1</sup>, Alexander N. Bugrov <sup>2,3</sup>, Iana A. Minich <sup>1</sup>, Ekaterina N. Malygina <sup>1</sup> and Irina A. Zvereva <sup>1</sup>

<sup>1</sup> Department of Chemical Thermodynamics and Kinetics, Institute of Chemistry, Saint Petersburg State University, 198504 Saint Petersburg, Russia; st062003@student.spbu.ru (V.V.V.); st040572@student.spbu.ru (S.A.K.); i.rodionov@spbu.ru (I.A.R.); st048953@student.spbu.ru (I.A.M.); st805605@student.spbu.ru (E.N.M.); irina.zvereva@spbu.ru (I.A.Z.)

<sup>2</sup> Department of Physical Chemistry, Saint Petersburg Electrotechnical University (ETU "LETI"), ul. Professora Popova 5, 197376 Saint Petersburg, Russia; alexander.n.bugrov@gmail.com

<sup>3</sup> Institute of Macromolecular Compounds, Russian Academy of Sciences, Bolshoy pr-t 31, 199004 Saint Petersburg, Russia

\* Correspondence: oleg.silyukov@spbu.ru; Tel.: +7-9533568028



**Citation:** Voytovich, V.V.; Kurnosenko, S.A.; Silyukov, O.I.; Rodionov, I.A.; Bugrov, A.N.; Minich, I.A.; Malygina, E.N.; Zvereva, I.A. Synthesis of *n*-Alkoxy Derivatives of Layered Perovskite-Like Niobate  $\text{HCa}_2\text{Nb}_3\text{O}_{10}$  and Study of Their Photocatalytic Activity for Hydrogen Production from an Aqueous Solution of Methanol. *Catalysts* **2021**, *11*, 897. <https://doi.org/10.3390/catal11080897>

Academic Editors: Trong-On Do and Panagiotis G. Smirniotis

Received: 2 July 2021

Accepted: 22 July 2021

Published: 25 July 2021

**Publisher's Note:** MDPI stays neutral with regard to jurisdictional claims in published maps and institutional affiliations.



**Copyright:** © 2021 by the authors. Licensee MDPI, Basel, Switzerland. This article is an open access article distributed under the terms and conditions of the Creative Commons Attribution (CC BY) license (<https://creativecommons.org/licenses/by/4.0/>).

**Abstract:** A series of hybrid inorganic–organic niobates  $\text{HCa}_2\text{Nb}_3\text{O}_{10} \times \text{ROH}$ , containing *n*-alkoxy groups of primary alcohols (R = Me, Et, Pr, Bu, Hx, and Dc) grafted in the interlayer space, has been studied for the first time in relation to photocatalytic hydrogen generation from a model 1 mol % aqueous solution of methanol under ultraviolet irradiation. Photocatalytic activity was measured both for bare samples and for their composites with Pt nanoparticles as a cocatalyst. The advanced measurement scheme allowed monitoring the volume concentration of a sample in a suspension during the experiment, its pH, and possible exfoliation of layered compounds into nanolayers. In the series of *n*-alkoxy derivatives, the maximum rate of hydrogen evolution was achieved over a Pt-loaded ethoxy derivative  $\text{HCa}_2\text{Nb}_3\text{O}_{10} \times \text{EtOH}/\text{Pt}$ . Its apparent quantum efficiency of 20.6% in the 220–350 nm range was found not to be caused by changes in the light absorption region or specific surface area upon ethanol grafting. Moreover, the amounts of hydrogen released during the measurements significantly exceeded those of interlayer organic components, indicating that hydrogen is generated from the reaction solution rather than from the hybrid material.

**Keywords:** photocatalysis; hydrogen; layered; perovskite; niobate; alcohols; grafting; inorganic-organic hybrid

## 1. Introduction

Heterogeneous photocatalysis is a promising environmentally friendly way for hydrogen production from various aqueous media. Since the overall photocatalytic splitting of pure water under sunlight is known to be a hardly feasible process due to thermodynamic and kinetic reasons [1–7], much attention is paid to obtaining hydrogen from the solutions of plant biomass processing products (bioalcohols, carbohydrates, etc.). The photocatalytic transformation of biomass into hydrogen with its further use as fuel should demonstrate much greater energy efficiency as compared with direct biomass combustion, since the latter has relatively low calorific value [8–17]. Moreover, photocatalysis may simultaneously serve as a destructive method for water purification from organic pollutants [18–21] whose decomposition is accompanied by hydrogen evolution.

Currently, the most investigated heterogeneous photocatalysts for hydrogen generation are materials based on simple wide-gap semiconductor oxides, chalcogenides, and

nitrides ( $\text{TiO}_2$ ,  $\text{Nb}_2\text{O}_5$ ,  $\text{WO}_3$ ,  $\text{CdS}$ ,  $\text{MoS}_2$ ,  $\text{Ge}_3\text{N}_4$ , etc.) [22,23]. However, their activity often turns out to be insufficient for practical use due to strongly pronounced electron–hole recombination, small specific surface and other factors, which justifies a continuous search for new photocatalytic materials.

Among promising photocatalysts, in recent decades, special attention has been paid to the class of ion-exchangeable layered perovskite-like oxides whose structure can be described as a regular alternation of negatively charged intergrowth blocks with a thickness of  $n$  corner-shared perovskite octahedra and interlayer spaces containing alkali cations. In accordance with structural features, these oxides may be classified into two groups: the Dion–Jacobson phases  $A[A_{n-1}B_nO_{3n+1}]$  and the Ruddlesden–Popper phases  $A'_2[A_{n-1}B_nO_{3n+1}]$ , where  $A'$  is an interlayer alkali cation,  $A$  = alkaline earth or transition cation,  $B$  = Nb, Ta, Ti, Zr, etc.) [24–26]. The enhanced photocatalytic activity of layered perovskites in the reactions of water and aqueous solutions decomposition is associated with their propensity for ion exchange [27–36] and intercalation [37–39], including the reversible introduction of relatively small reactants into the interlayer space during photocatalysis [35,40,41]. Particularly, the perovskites' interlayer space is supposed to act as a separate reaction zone containing reaction centers of a fundamentally new type, which are different from those located on the external surface [42]. The main methods for the improvement of photocatalytic activity of layered perovskites presented in the literature are doping with various elements [43–47], intercalation of metals [48–50], the creation of composite materials [51–54], including Z-schemes [55–59], photosensitization [60–64] as well as exfoliation into nanosheets [65].

An important feature of layered perovskite-like oxides consists in the ability of their protonated forms ( $A' = \text{H}$ ) to react with some organic compounds, giving so-called inorganic–organic derivatives (or inorganic–organic hybrids) representing the products of organic components insertion into the interlayer space [66–68]. The formation of these hybrid materials may proceed as either the intercalation of organic bases (amines [69–72], aminoalcohols [73,74], aminoacids [75], etc.) or esterification-like grafting, which is typical of reactions with alcohols [76–79], carbohydrates [80], alkoxy silanes [81], and organophosphorus acids [82]. Despite a large number of known inorganic–organic derivatives of perovskite-like oxides, their photocatalytic properties were given much less attention, which may be connected with their expected instability under the photocatalysis conditions. For instance, the modification of the tantalate  $\text{HCa}_2\text{Ta}_3\text{O}_{10}$  with  $n$ -hexylamine [83] was found to greatly increase its photocatalytic activity toward water splitting under ultraviolet light. However, the activity drastically reduced a few hours after the measurement beginning, which was caused by the amine oxidation and further interlayer space constriction. The authors of another paper [84] reported on the enhanced photocatalytic activity of the tantalate  $\text{H}_2\text{CaTa}_2\text{O}_7$  containing grafted  $n$ -alkoxy groups with regard to light-driven degradation of aqueous rhodamine and methyl orange and revealed that the activity was increasing as a hydrocarbon chain length was rising. Our recent report on the photocatalytic activity of the titanate  $\text{H}_2\text{Nd}_2\text{Ti}_3\text{O}_{10}$  intercalated by  $n$ -butylamine [85] showed its significant superiority over the unmodified compound with respect to hydrogen generation from aqueous  $n$ -alcohols as well as pure water.

Layered perovskite-like niobate  $\text{HCa}_2\text{Nb}_3\text{O}_{10}$  is a protonated form of the Dion–Jacobson phases  $\text{ACa}_2\text{Nb}_3\text{O}_{10}$  ( $A$  = alkali cation) whose structure consists of alternating perovskite slabs with a thickness of  $n = 3$  niobium–oxygen octahedra separated by interlayer spaces populated by singly charged cations. It could be obtained by the ion exchange of interlayer cations  $A^+$  for protons [29,33]. This compound is known to exist in a hydrated form  $\text{HCa}_2\text{Nb}_3\text{O}_{10} \cdot 1.5\text{H}_2\text{O}$ , demonstrating high reactivity toward direct intercalation [39] and grafting [76] reactions with organic substances. The present research, devoted to  $n$ -alkoxy derivatives of the niobate in question, is a continuation of our recent study on the photocatalytic properties of the  $n$ -alkylamine ones [86]. As shown, their activity correlates with the hydration degree of the interlayer space, and the most active  $n$ -butylamine derivative after platinumization provides apparent quantum efficiency of hydrogen production of

13%. As in the previous research, here, special attention is paid to the comprehensive analysis of hybrid compounds and their stability under photocatalytic conditions.

## 2. Results and Discussion

### 2.1. Identification of the Initial and Protonated Niobates

Initial alkaline layered perovskite-like niobate  $\text{KCa}_2\text{Nb}_3\text{O}_{10}$  ( $\text{KCN}_3$ ) and its protonated hydrated form  $\text{HCa}_2\text{Nb}_3\text{O}_{10} \cdot y\text{H}_2\text{O}$  ( $\text{HCN}_3 \cdot y\text{H}_2\text{O}$ ) were identified by the XRD analysis. Tetragonal lattice parameters of the samples ( $a = 3.86 \text{ \AA}$ ,  $c = 29.4 \text{ \AA}$  for the former and  $a = 3.82 \text{ \AA}$ ,  $c = 16.0 \text{ \AA}$  for the latter) were shown to be in good consistency with the literature values [29,87]. The distance between the centers of adjacent perovskite slabs (interlayer distance  $d$ ) increases upon the formation of  $\text{HCN}_3 \cdot y\text{H}_2\text{O}$  from  $\text{KCN}_3$  because of water intercalation. The  $c$  parameter of the alkaline form is doubled toward  $d$ , which does not take place in the case of the protonated form. Hence, the protonation reaction is accompanied by a change in a perovskite slabs' conformation from staggered to eclipsed. According to the TG analysis, the  $\text{HCN}_3 \cdot y\text{H}_2\text{O}$  obtained contains about 1.5 water molecules per structural unit and represents a fully protonated compound with a substitution degree of  $\text{K}^+$  cations for protons  $\text{H}^+$  close to 100%.

### 2.2. Analysis of the Inorganic–Organic Compounds

The XRD patterns of the hybrid inorganic–organic compounds presented in Figure 1 confirm the successful preparation of all the samples in a single-phase state without noticeable amounts of impurities. All the reflections observed can be successfully indexed in the tetragonal system. The introduction of  $n$ -alkoxy groups into the interlayer space leads to its noticeable expansion, which is confirmed by the characteristic shift of the reflections ( $00l$ ) in the low-angle region. This shift corresponds to a change in the  $c$  lattice parameter of the tetragonal cell, which is perpendicular to the plane of the oxide layers. From a physical point of view, this shift is caused by an increase in the distance between adjacent perovskite layers due to the incorporation of bulky organic molecules. The magnitude of the shift is proportional to the organic component chain length. At the same time, sizes of niobium-oxygen octahedra are retained, since the  $a$  lattice parameter practically does not change. XRD patterns of all the inorganic–organic compounds, with the exception of the methoxy one, are amenable to indexing without doubling the  $c$  parameter, which seems to indicate the eclipsed conformation of their slabs. The lower intensity of the ( $00l$ ) reflections on the patterns of the hybrid inorganic–organic compounds may be due to lowering the crystal ordering upon the insertion of organic components between perovskite layers.

The dependence of the interlayer distance  $d$  calculated from the  $c$  lattice parameter of the tetragonal cell (Figure 2a) of the hybrids on the alkyl chain length ( $n_C$ ) of an organic component is shown in Figure 2b, where  $n_C = 0$  corresponds to the unmodified hydrated protonated niobate,  $n_C = 1$  – to the methoxy derivative, etc. Linear fitting of experimental points does not connect the former two because the interlayer distance  $d$  of the protonated niobate is larger than that of the methoxy derivative. Apparently, this fact is observed due to strong extension of the interlayer space by water molecules. It is also possible to estimate an average angle between organic chains and perovskite slabs using the following assumptions: *all-trans*-conformations of interlayer organic components, parallelism of the chains to each other, and constant length of the chain overlapping (a model of tilted bilayer is presented in Figure 2c). The slope of the linearized  $d = d(n_C)$  dependence and a hypothetical chain elongation with the introduction of a  $-\text{CH}_2-$  group  $1.27 \text{ \AA}$  [39] should also be taken into account. Thus, the inorganic–organic hybrids prepared have a paraffin-like organic bilayer with an average slope of  $57^\circ$ . Hence, the angle values found for the Dion–Jacobson niobates in question are less than those determined for organically modified Ruddlesden–Popper titanates [69,71,79].

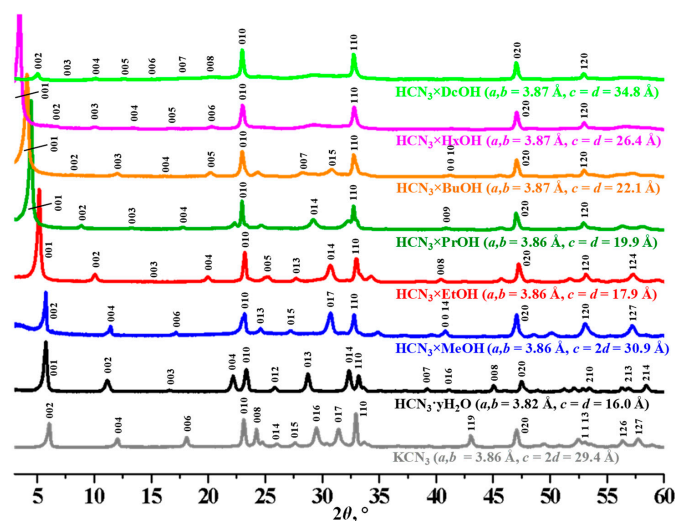


Figure 1. XRD patterns of the initial niobates and *n*-alkoxy derivatives.

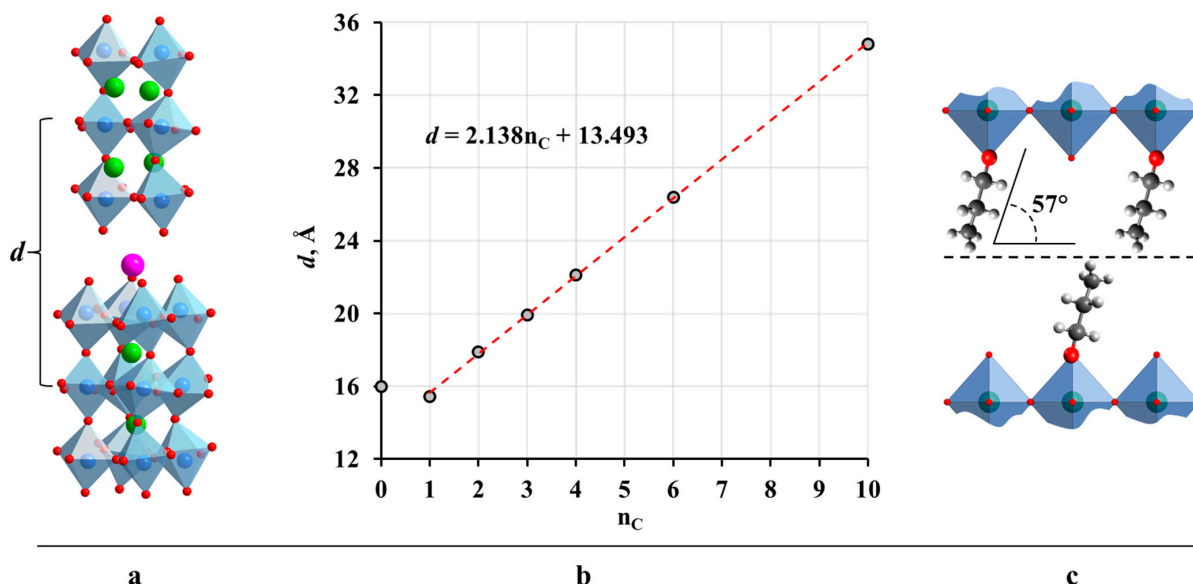
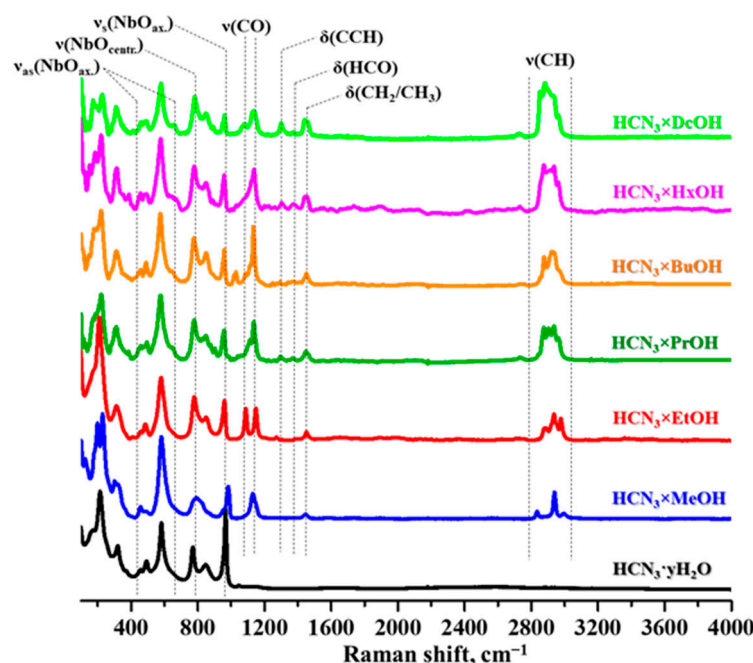


Figure 2. Crystal structure fragment of initial KCN<sub>3</sub> (a), correlation between the interlayer distance  $d$  and *n*-alkoxy chain length (b), model of a paraffin-like tilted organic bilayer (c).

Raman spectra of the hybrids (Figure 3) consist of vibrational bands of the perovskite matrix (100–1000 cm<sup>-1</sup>) [88,89] and organic components (1000–4000 cm<sup>-1</sup>). One can observe the latitudinal vibrations of C–C–H (1300 cm<sup>-1</sup>), H–C–O (1370 cm<sup>-1</sup>), and CH<sub>2</sub>/CH<sub>3</sub> (1450–1470 cm<sup>-1</sup>) fragments as well as C–H stretching (2800–3050 cm<sup>-1</sup>). At the same time, the spectral region of 50–1000 cm<sup>-1</sup> does not undergo substantial changes in the course of the organic modification, which indicates that NbO<sub>6</sub> octahedra are not strongly affected by the organic components inserted.

Special attention should be paid to the bands in the range of 1050–1150 cm<sup>-1</sup> (single band in the spectrum of the methoxy derivative and two bands in other cases). Comparison of the hybrids' spectra (Figure 3) with those of initial molecular *n*-alcohols (not shown) allows suggesting that the aforementioned bands relate to complex vibrations of inserted organic components involving the C–O bond stretching designated as  $\nu(\text{CO})$ . However, in the case of the inorganic–organic derivatives under consideration, these bands are shifted by 50–100 cm<sup>-1</sup> toward a high-frequency region and have a very high intensity being comparable to the intensity of the C–H bands (in the spectra of molecular *n*-alcohols, the C–O bands are 5–10 times less intense than the C–H ones). The facts mentioned

indicate that the interlayer space of the derivatives actually contains not intercalated *n*-alcohol molecules but their *n*-alkoxy groups covalently bonded to perovskite slabs. When moving from molecular alcohols to the grafted ones, a chain of chemical bonds C–O–H turns into C–O–Nb including the heavy Nb cation, which leads to an increase in the C–O stretching frequency. Apparently, the C–O vibrations in the perovskite matrix also involve a significantly more pronounced change in the polarizability of the C–O bond than in a molecular alcohol, due to which the corresponding bands in the hybrids' Raman spectra have a much higher intensity. Another important fact pointing at successful grafting is the absence of the OH-group bands (3100–3500 cm<sup>-1</sup>) that are presented in the spectra of molecular *n*-alcohols.



**Figure 3.** Raman spectra of the protonated niobate and its *n*-alkoxy derivatives.

The <sup>13</sup>C NMR solid-state spectra of the hybrid samples, shown in Figure 4, also confirm the successful obtainment of grafted inorganic–organic compounds. All the bands observed can be referred to the carbon atoms of target *n*-alkoxy groups, which also proves the absence of ethanol and *n*-propanol (or their alkoxy fragments) in the samples with the longer alkyl chains whose syntheses involved using ethoxy and *n*-propoxy derivatives as precursors. In the spectra of the long-chain derivatives (R = Hx, Dc), overlapping of some bands is observed. In particular, middle carbon atoms (4, 5 in the *n*-hexoxy derivative and 4–9 in the *n*-decoxy one) have similar electron shielding, which explains the close chemical shifts of their bands and, consequently, the overlapping mentioned. This phenomenon is not pronounced in the case of shorter *n*-alkoxy groups (R = Et, Pr, Bu), since their carbon atoms differ more from each other in terms of electronic shielding. The bands of carbon atoms adjacent to oxygen are shifted by 15–20 ppm in a weak field relative to the corresponding bands in the spectra of molecular alcohols, which strongly proves the covalent nature of the bond between the inorganic matrix and organic components. In the case of the ethoxy derivative, the spectrum also demonstrates a low-intensity band at 57 ppm that probably belongs to molecular ethanol residues.

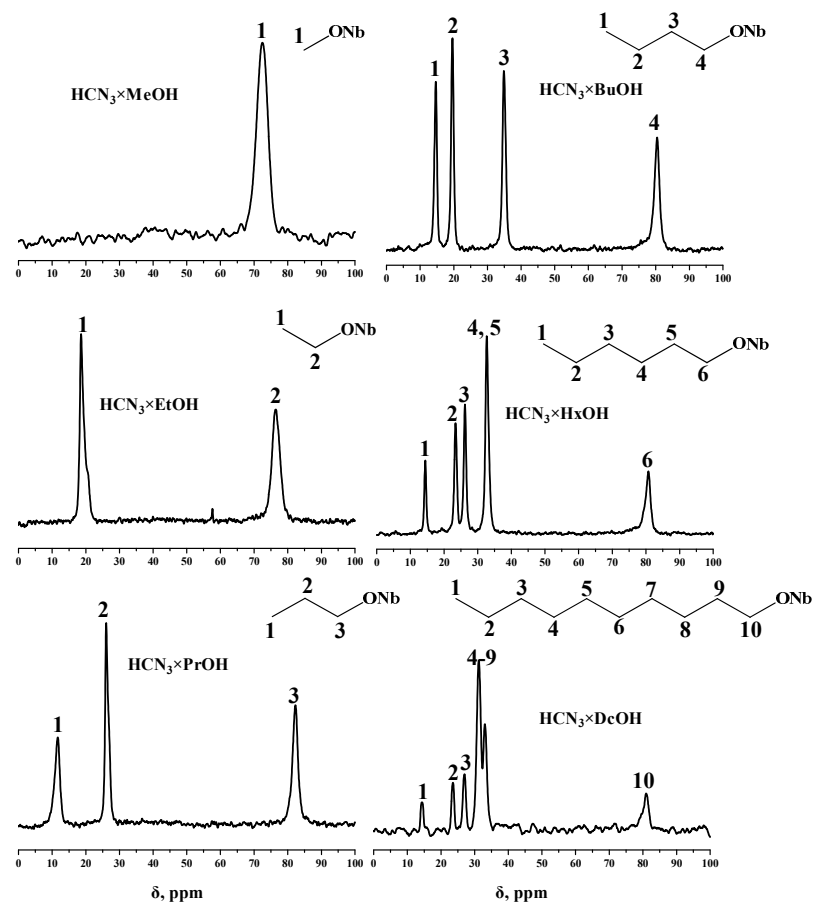


**Figure 4.**  $^{13}\text{C}$  NMR spectra of the *n*-alkoxy derivatives.

Quantitative compositions of the hybrids (Table 1) were established using elemental CHN-analysis and TG according to a two-stage scheme. At the first stage, the data from CHN-analysis were used to determine the mass content of carbon in the sample. Then, based on the assumption that all of the carbon detected belongs to the grafted alcohol molecules, the mass content of the organic component in the sample was calculated. At the second stage, thermogravimetric data were used to calculate the total mass loss of the samples in the course of heating on air. Taking into account the fact that the final state of the inorganic part after complete decomposition in an oxidizing atmosphere corresponds to the composition of  $\text{Ca}_2\text{Nb}_3\text{O}_{9.5}$  and knowing the mass of the organic component in the sample, it was possible to calculate the content of intercalated water ( $y$ ) and organic content ( $x$ ) based on the generalized formula of the hybrids  $x(\text{RO})\text{H}_{1-x}\text{Ca}_2\text{Nb}_3\text{O}_{10-x} \cdot y\text{H}_2\text{O}$ . All the hybrids obtained contain 0.8–1.0 corresponding organic components per structural unit of the niobate as well as some amount of intercalated water. As one can see, the ethoxy derivative is characterized by the greatest hydration degree ( $y = 0.45$ ). In the case of long-chain substituents ( $R = \text{Hx}, \text{Dc}$ ), the degree of hydration is seen to be relatively low. This fact can be explained by the synthesis of these samples in non-aqueous solutions. The source of water in long-chain hybrids is the ethoxy derivative, which acts as a precursor during their synthesis. The decrease in the water amount may be due to the high temperatures used for the grafting. Under strong heating, the water leaves the interlayer space, despite the fact that there is mixing of molecules with different polarity in the reaction medium. In the case of short-chain substituents ( $R = \text{Me}, \text{Et}, \text{Pr},$  and  $\text{Bu}$ ), a greater amount of water in the interlayer space of the hybrids may be associated with the smaller difference in polarity between interlayer *n*-alkoxy chains and water molecules. In the case of methoxy and ethoxy derivatives, the lower synthesis temperature and the presence of water in the reaction mixture could have played a significant role, too. The methoxy hybrid has a shorter

interlayer distance  $d$  compared to that of the hydrated protonated niobate and contains 1.05 interlayer methoxy groups per formula unit. Based on this, it can be concluded that all interlayer protons in this hybrid are replaced by organic groups and the introduction of additional water to expand the interlayer space is difficult. Therefore, the degree of hydration is low. On the contrary, the hydration degree of the ethoxy hybrid is the highest, which can be explained by a simultaneous influence of at least two factors: relatively high polarity of an ethoxy group and sufficient interlayer distance for a larger number of water molecules.

**Table 1.** Quantitative compositions, light absorption regions, and specific surface areas of the samples. The compositions are presented in the form  $x(\text{RO})\text{H}_{1-x}\text{Ca}_2\text{Nb}_3\text{O}_{10-x}\cdot y\text{H}_2\text{O}$ .

Sample	Composition		Light Absorption		Specific Surface, m <sup>2</sup> /g	
	x	y	E <sub>g</sub> , eV	λ <sub>max</sub> , nm	N <sub>2</sub>	Kr
KCN <sub>3</sub>	–	–	3.54	350	3.8	4.4
HCN <sub>3</sub> ·yH <sub>2</sub> O	–	1.5	3.50	354	5.6	7.6
HCN <sub>3</sub> ×MeOH	1.00	0.20	3.45	359	2.4	2.9
HCN <sub>3</sub> ×EtOH	0.90	0.45	3.50	354	4.7	3.9
HCN <sub>3</sub> ×PrOH	0.85	0.35	3.53	351	6.4	6.1
HCN <sub>3</sub> ×BuOH	0.85	0.40	3.50	354	7.3	7.4
HCN <sub>3</sub> ×HxOH	0.85	0.20	3.47	357	10.7	13.8
HCN <sub>3</sub> ×DcOH	0.90	0.25	3.51	353	10.2	13.2

Diffuse reflectance spectra of the inorganic–organic hybrids prepared as well as Tauc plots for determining the optical bandgap values E<sub>g</sub> are presented in Supporting Information S1. Light absorption in the absence of impurities occurs due to interband transitions in the near ultraviolet range and, therefore, the color of the powders is white. It can be seen that the interlayer modification of the niobate with *n*-alkoxy groups neither affects the general appearance of the spectrum nor gives new absorption bands. A decrease in the bandgap energy upon the incorporation of organic components does not exceed 0.09 eV and depends on the chain length non-monotonically (Table 1). Usually, increasing of the interlayer distance  $d$  leads to a noticeable growth of bandgap energy [90]. Apparently, introduced organic components reduce the E<sub>g</sub> value, offsetting the inverse effect associated with the variation of the  $d$  parameter described below. Nevertheless, substantial differences in photocatalytic activity of the unmodified niobates and inorganic–organic derivatives cannot be accounted for different regions of light absorption.

Specific surface area, conversely, sharply decreases when moving from the protonated niobate to the methoxy derivative and then monotonously increases with an increase in the length of the interlayer *n*-alkoxy group (Table 1). The dependence of the specific surface area on the alkyl chain length is reaching a plateau for the long-chain derivatives. It is worth noting that the BET method does not work accurately enough for samples with such a low specific surface area, due to which the values measured with N<sub>2</sub> and Kr as adsorbates can differ significantly from each other. Nevertheless, the general pattern is evident.

The results of SEM showed that all the hybrids obtained are generally similar in morphology both to each other and to the initial compounds (Figure 5). The particles of the samples have a plate-like shape and their dimensions are, on average, 150–300 nm in thickness and 500–800 nm in length. Moreover, for *n*-hexoxy and *n*-decoxy hybrids, partial stratification is clearly observed. This fact can be explained by the influence of long organic chains on the layered structure and is consistent with the values of the specific surface area, which were found to be the highest for the long-chain derivatives (Table 1).

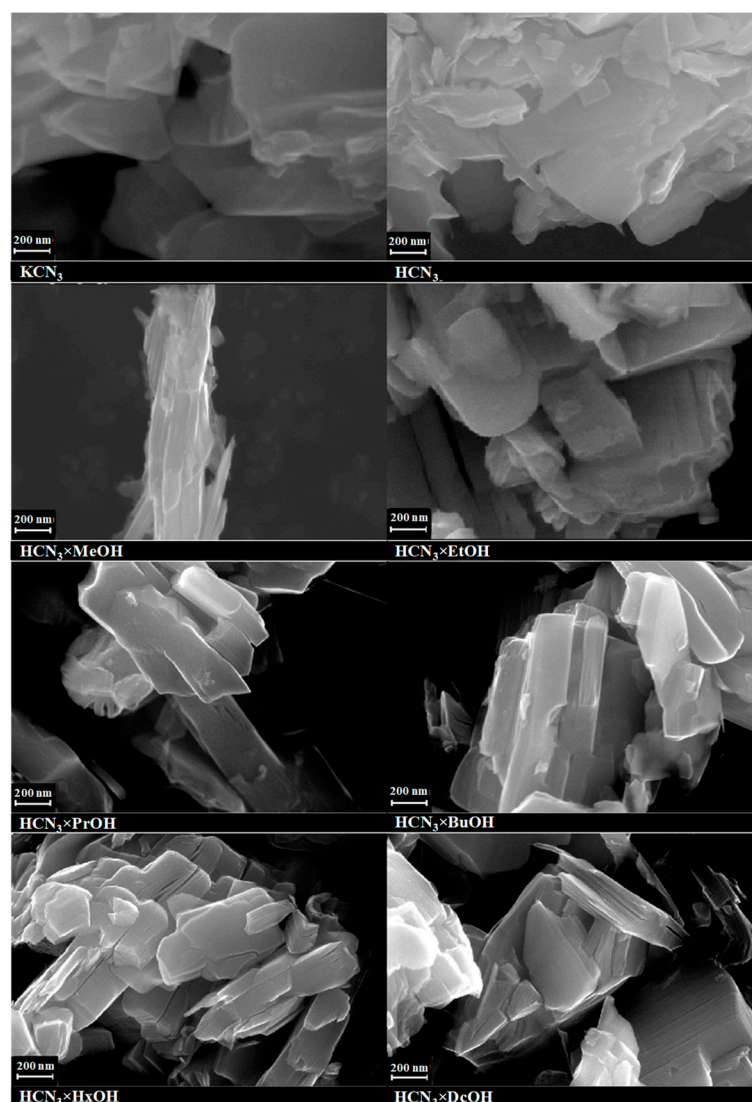


Figure 5. SEM images of the initial niobates and their  $n$ -alkoxy derivatives.

### 2.3. Thermal, Vacuum, and Hydrolytic Stability of the Inorganic–Organic Hybrids

TG curves of the initial protonated niobate and hybrid derivatives measured in an oxidative atmosphere are shown in Figure 6. Thermal degradation of the protonated compound includes two stages. The first stage refers to temperatures lower than 275 °C and corresponds to the deintercalation of water from the interlayer space with the formation of a dehydrated niobate. The second stage (275–450 °C) relates to topochemical condensation that consists in the combination of interlayer oxygen and hydrogen into water molecules. The release of the latter is accompanied by the closure of adjacent perovskite blocks.

The thermal decomposition of the hybrids is a more complex process. Based on the behavior of the mass loss curves and data on the line of  $n$ -alkylamine derivatives of  $\text{HCa}_2\text{Nb}_3\text{O}_{10}$  reported earlier [86], the following mechanism can be assumed. The first section of the curves (approximately 50–225 °C) refers to the deintercalation of water from the interlayer space as well as the removal of intercalated molecular alcohols or adsorbed washing solvents (if there are any). However, grafted  $n$ -alkoxy groups appear to retain at these temperatures. At the second section of the curves, further heating is accompanied by a mass loss associated with the organic component decomposition and elimination of water and carbon dioxide, which is followed by the mass gain due to partial oxidation of the carbon-containing compound (the main part of carbon remains in the sample at this stage). As in the case of other inorganic–organic perovskite-like compounds, the

carbon residue completely burns out with the formation of carbon dioxide and a solid residue in the high-temperature region (550–950 °C). Due to the covalent nature of bonding between the organic component and niobium–oxygen octahedra, molecular alcohols are not released during the thermolysis of the hybrids. Moreover, the covalent bonding provides relatively high thermal stability of the *n*-alkoxy derivatives in comparison with that of the *n*-alkylamine ones [86], which makes it possible to manipulate the samples in a wider temperature range as well as to purposefully dehydrate them if necessary.

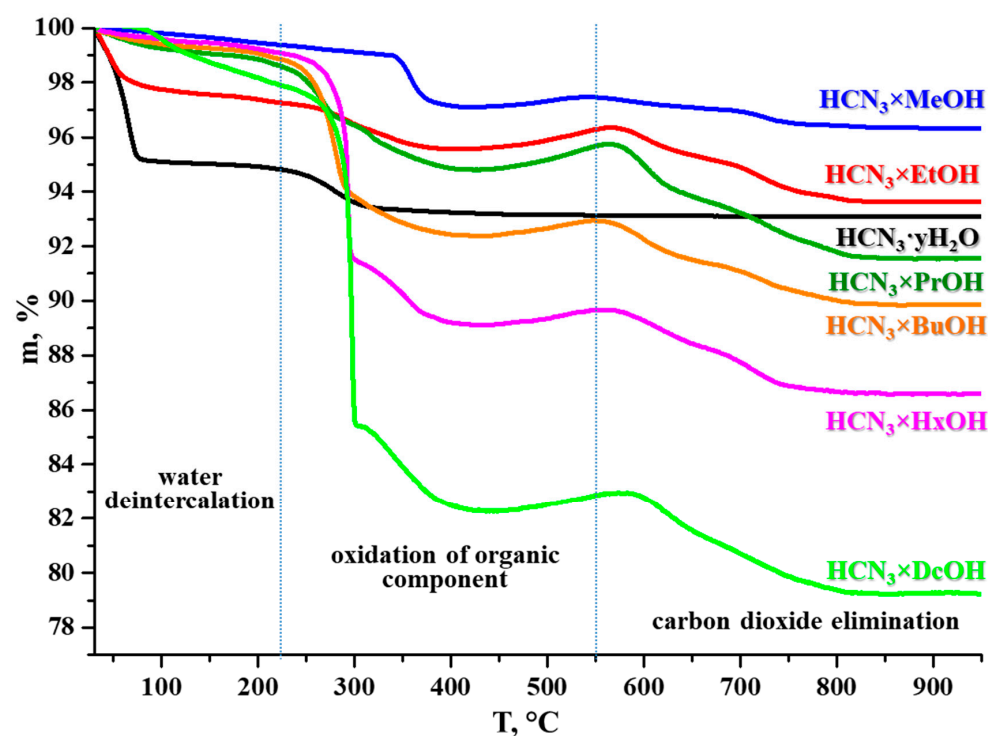


Figure 6. TG curves of the protonated niobate and its *n*-alkoxy derivatives.

All the *n*-alkoxy hybrids obtained were tested for vacuum stability. This study was necessary in connection with the use of BET and SEM methods involving deep evacuation of the samples being analyzed. The results of the CHN-analysis of initial and vacuum-cured inorganic–organic samples (Supporting information S2) showed that the organic content in most of them preserves even after long keeping under deep vacuum ( $1 \times 10^{-4}$  atm). The substantial loss in organic content ( $\approx 0.2$  ethoxy groups per structural unit) was revealed for the ethoxy derivative. This fact may be due to the presence of residual loosely bound molecular ethanol (band at 58 ppm in the NMR spectrum) in the interlayer space that easily liberates under reduced pressure. Thus, the presence of intercalated ethanol explains not only the loss of a noticeable amount of the organic component under evacuation but also the large mass loss in the low-temperature region on the TG curve.

All the hybrids were also tested for stability toward the hydrolysis of *n*-alkoxy groups in aqueous solutions (Supporting Information S3) that is the reverse reaction in relation to grafting and hypothetically should lead to the formation of the initial protonated niobate. Most of the hybrids ( $R = Et-Hx$ ) after 1 d of water treatment noticeably change the appearance of their XRD patterns. However, even after 10 d of water treatment, complete coincidence of the hybrids' patterns with that of the protonated niobate is not observed. The XRD patterns of many water-treated samples are generally similar to each other. The crystal structure of the methoxy derivative, which appeared to be the most stable toward the water influence, is seen to be fully retained after 1 d treatment. After 10 d, the resulting sample shows the formation of a second phase with a greater interlayer distance  $d$  and may represent a hydrated form of the methoxy derivative. In the case of the *n*-decoxy derivative, the XRD patterns after 1 and 10 d treatment are similar to each other. Despite the

aforementioned changes in the structure of all the hybrids, which are apparently associated with a constriction of the interlayer space, Raman spectra clearly confirm the presence of the organic component in all of them even after 10 d holding in water (Supporting Information S4). However, ethoxy, *n*-propoxy, *n*-butoxy, and *n*-hexoxy derivatives demonstrate 2–3 times lower intensities of C–H stretching bands in comparison with those of the initial hybrids, which may point at the partial hydrolysis of their *n*-alkoxy groups with the formation of *n*-alcohols further leaving the interlayer space. In the case of methoxy and *n*-decoxy samples, the corresponding vibrational bands preserve their intensities, suggesting that the amount of the organic component in these compounds remains practically unchanged. With this in mind, the structural changes demonstrated by XRD patterns of these two samples are rather caused not by washout of organic modifiers but by additional interlayer hydration and a subsequent change in the conformation (for instance, slope) of the alkoxy chains.

#### 2.4. Photocatalytic Activity of the Hybrid Inorganic–Organic Niobates

The photocatalytic activity of the *n*-alkoxy derivatives was investigated toward hydrogen evolution from the model 1 mol % methanol solution in water. Kinetic curves of hydrogen generation for bare (Figure 7) and for platinized samples (Figure 8) demonstrate almost linear behavior, indicating that the photocatalytic activity of most inorganic–organic derivatives stably maintains throughout the whole measurement time. Analysis of the dark stages allows one to conclude that the reactions of hydrogen generation for all the compounds in question are indeed photocatalytic, not just photoinitiated, since, in the absence of irradiation, the curves reach a plateau corresponding to a zero reaction rate.

The photocatalytic activity of the initial alkaline and protonated niobates in the absence of a cocatalyst is relatively low. The calculated apparent quantum efficiency is  $\varphi = 0.0125\%$  for the alkaline and  $\varphi = 0.172\%$  for the protonated niobate, respectively (Table 2). A significant increase in the activity going from the alkaline to protonated form is probably explained by the fact that the protonated form exists in a highly hydrated state, while the alkaline one does not intercalate water at all [33]. According to the literature data [35,40,85,86], interlayer water actively participates in photocatalytic hydrogen generation. The alkaline niobate is not hydrated and, therefore, turns out to be inactive. The pH factor can also affect the photocatalytic activity observed. A weakly acidic pH of the suspension of the protonated form could be more favorable for photocatalysis than an alkaline pH provided by the potassium niobate (Supporting Information S5) [7]. However, the photocatalytic activity of the protonated niobate under consideration is much higher than that of protonated triple-layer Ruddlesden–Popper titanates tested in the same conditions [85]. This difference is explained by the existence of the protonated titanates in a much less hydrated state in comparison with the niobate. However, the alkaline forms of the titanates are more active than the alkaline niobate, since the former exist in a partially protonated and hydrated state, while the alkaline niobate is neither protonated nor hydrated in aqueous media, as mentioned above [85]. Platinization of the niobate surface leads to an increase in the activity by an order of magnitude ( $\varphi = 0.11\%$  for the alkaline and  $\varphi = 7.8\%$  for the protonated form). Pt nanoparticles on the compounds' surface significantly enhance the efficiency of spatial charge separation and simultaneously serve as hydrogen formation active sites [13].

All the inorganic–organic hybrids prepared demonstrate much higher photocatalytic activity compared to that of the alkaline and protonated niobates (Table 2). In the series of bare derivatives (without Pt cocatalyst), the most active members are *n*-butoxy, *n*-hexoxy, and *n*-decoxy derivatives ( $\varphi = 1.1$ – $1.7\%$ ) that demonstrate quantum efficiency that is more than 10 times higher in comparison with that of the protonated niobate. The bare *n*-alkoxy derivatives are 27–45 times more active than the “classic” photocatalyst TiO<sub>2</sub> P25 Degussa ( $\varphi = 0.039\%$ ). After platinization, the difference in the activity between the hydrated protonated niobate and hybrids falls sharply: even the most active ethoxy compound ( $\varphi = 20.6\%$ ) was found to be only 2.6 times more active than the hydrated protonated form

( $\phi = 7.83\%$ ). Photocatalytic activity of the rest of the platinumized hybrids falls in range of  $\phi = 10.6\text{--}15.4\%$ .

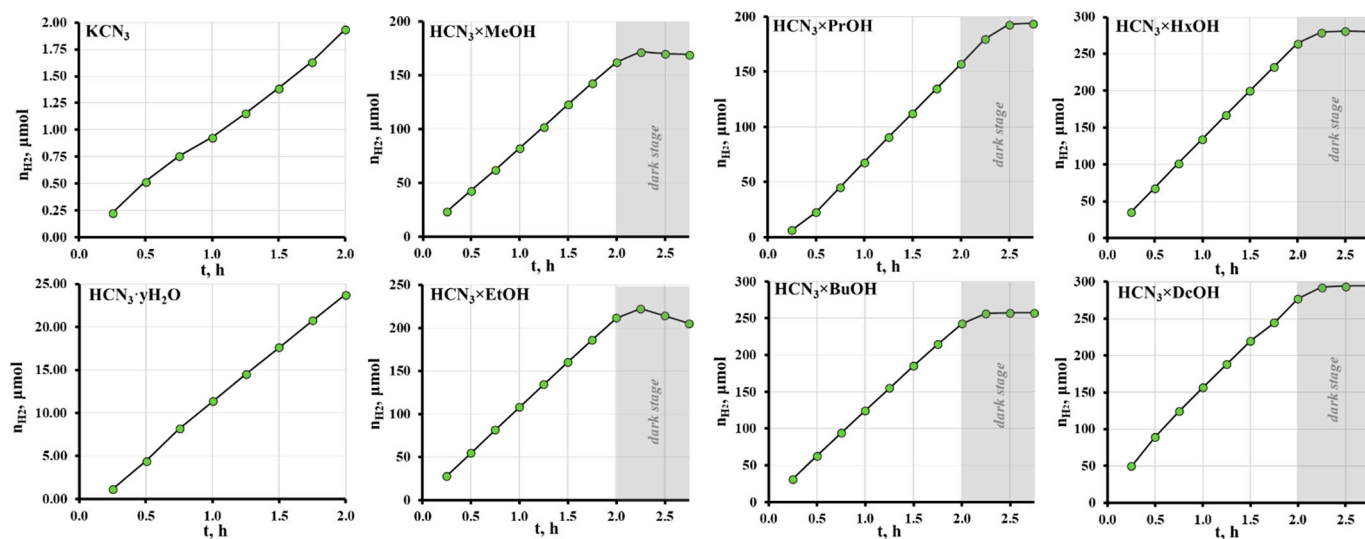


Figure 7. Kinetic curves of photocatalytic hydrogen generation over bare initial niobates and their *n*-alkoxy derivatives.

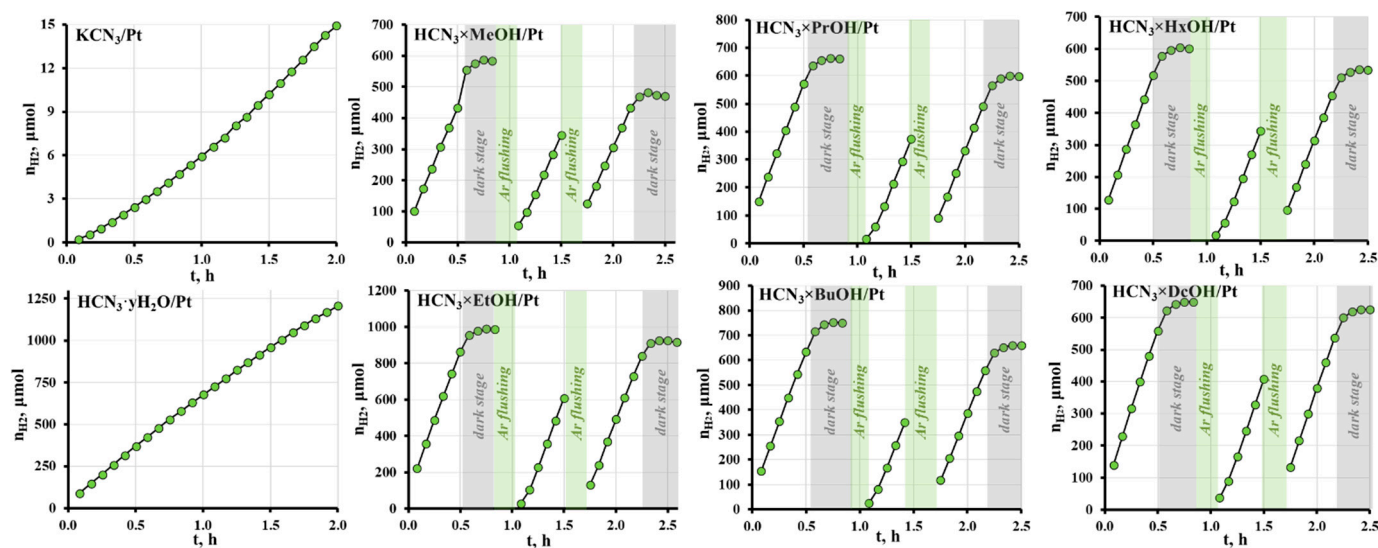


Figure 8. Kinetic curves of photocatalytic hydrogen generation over initial niobates and their *n*-alkoxy derivatives with a Pt cocatalyst.

Table 2. Data on photocatalytic activity of the initial niobates and their *n*-alkoxy derivatives (hydrogen evolution rate  $\omega$ , apparent quantum efficiency  $\phi$ , and platinumization increase factor  $k_{Pt}$ ).

Compound	Bare		Pt-Loaded		$k_{Pt}$
	$\omega$ , $\mu\text{mol/h}$	$\phi$ , %	$\omega$ , $\mu\text{mol/h}$	$\phi$ , %	
KCN <sub>3</sub>	0.94	0.013	7.8	0.11	8.40
HCN <sub>3</sub> ·yH <sub>2</sub> O	13	0.17	586	7.8	45.4
HCN <sub>3</sub> ×MeOH	80	1.1	796	10.6	10.0
HCN <sub>3</sub> ×EtOH	105	1.4	1544	20.6	14.7
HCN <sub>3</sub> ×PrOH	88	1.2	1009	13.5	11.5
HCN <sub>3</sub> ×BuOH	121	1.6	1151	15.4	9.50
HCN <sub>3</sub> ×HxOH	131	1.8	938	12.5	7.20
HCN <sub>3</sub> ×DcOH	128	1.7	1005	13.4	7.90

Summarizing, the highest photocatalytic activity has been established for the *n*-hexoxy derivative among bare samples and for the ethoxy derivative among Pt-loaded ones. In the line of bare samples, the trends observed can be explained by the value of the specific surface area that is the greatest for the *n*-hexoxy derivative and the least for the methoxy one, the first of which is the most active and the second is the least. The superior activity of the ethoxy derivative can be caused by the greatest amount of intercalated water, potentially participating in the target photocatalytic reaction. In particular, the activity of highly hydrated samples may be associated with the indirect oxidation of methanol following the next mechanism. A hole localized on the oxygen of the perovskite block takes an electron from an intercalated water molecule. As a result, a hydroxyl radical is formed, and it can subsequently oxidize an alcohol molecule. In general, the activity of highly hydrated samples correlates with the specific surface area (Figure 9) and interlayer hydration degree (Figure 10) in both lines of measurements (bare and Pt-loaded). Some organically modified samples have a smaller surface area but a higher photocatalytic activity than the original niobate. In addition, the multiplicity of the increase in the activity is not equal to the multiplicity of the increase in specific surface area. In other words, the developed surface area is important, but it is not the main factor determining the high activity of hybrids.

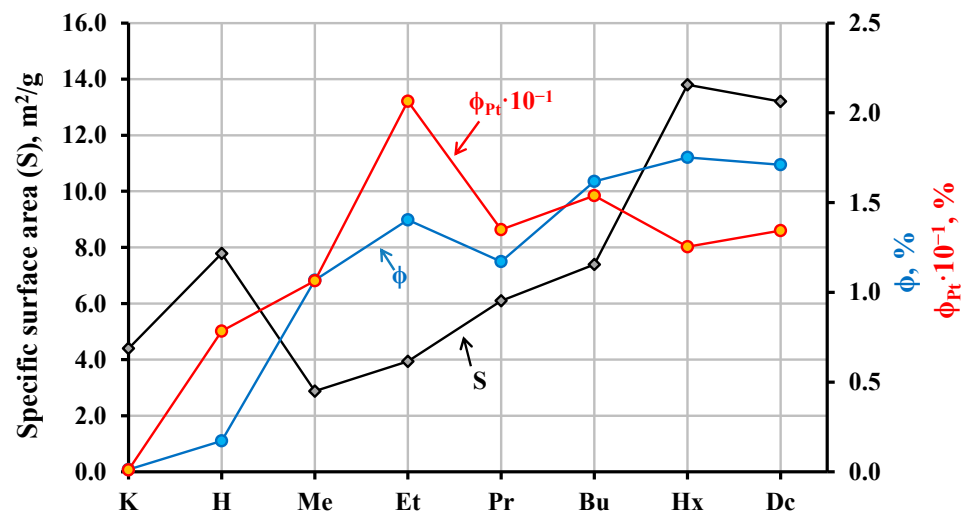


Figure 9. Correlation between apparent quantum efficiency  $\phi$  and specific surface area ( $K_r$ ) of the samples.

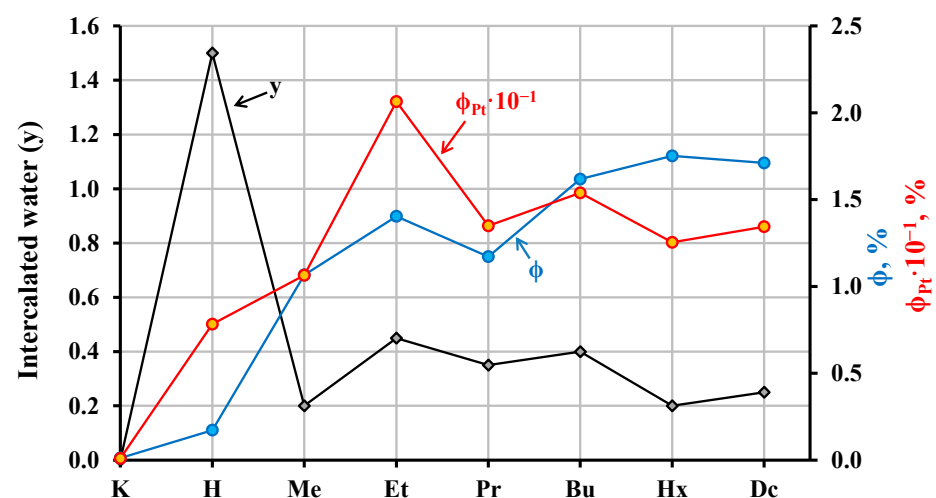


Figure 10. Correlation between apparent quantum efficiency  $\phi$  and hydration degree of the samples.

The results of the photocatalytic tests (Table 2) clearly show that the increase factor of the photocatalytic activity after platinization of the samples strongly depends on their nature ( $k_{Pt} = 7.20\text{--}45.4$ ). Its value is generally similar for the most samples ( $k_{Pt} = 7.20\text{--}14.7$ ), with the exception of the protonated form experiencing the strongest effect of platinization ( $k_{Pt} = 45.4$ ). The photocatalytic activity of bare samples and Pt-loaded ones does not always change symbotically when going from one compound to another. Moreover, the  $k_{Pt}$  coefficient correlates with the degree of interlayer hydration. Among all the compounds in question, the protonated niobate is the most hydrated. Its degree of hydration is higher than that of the ethoxy one by as many times as the  $k_{Pt}$  coefficient. Thus, the differences in the photocatalytic activity of the platinized samples cannot be interpreted only in light of different properties of bare samples taken by themselves. In other words, despite the general chemical nature of these samples, the same cocatalyst affects their activity differently. Apparently, the different effect of platinization is associated with the unequal efficiency of spatial charge separation, which directly affects the electron–hole recombination.

In the case of multistage photocatalytic measurements including flushings with argon, the rate of hydrogen generation slightly decreases after flushing (Figure 8), which can be explained by the violation of the sorption–desorption equilibrium of the reactants and products. Moreover, the amount of hydrogen released during the photocatalytic experiment significantly exceeds that of the interlayer organic component and, having said so, the rate of hydrogen generation remains the same. Thus, hydrogen is generated rather from the water–methanol solution than from the organic material of the hybrids.

As stated earlier, the rate of photocatalytic hydrogen evolution from aqueous solutions depends on the pH of a reaction medium. According to our measurements, the photocatalytic suspensions of the niobates show a weakly acidic reaction of the medium (Supporting Information S5), with the exception of the alkaline form  $KCN_3$ . In the case of the *n*-alkoxy derivatives, the corresponding pH values are associated with the presence of residual interlayer protons. Lower pH values in suspensions of *n*-alkoxy hybrids compared to those of *n*-alkylamine ones [86] can explain the greater activity of the former. Furthermore, the platinization of the samples provides additional pH decrease because the acid  $H_2PtCl_6$  serves as a source of Pt. The decrease in pH during the photocatalytic experiments ( $pH_1 > pH_2$ ), which is more pronounced in the case of highly active samples (for example,  $HCN_3 \times HxOH$ ,  $HCN_3 \times EtOH/Pt$ ), might be caused by the partial oxidation of methanol to formic acid.

Dispersibility of the oxide particles in the reaction medium was found to strongly depend on the interlayer organic component (Supporting Information S5). In particular, hybrids with short-chain *n*-alkoxy groups ( $R = Me, Et, Pr, \text{ and } Bu$ ) readily form suspensions in aqueous methanol, while long-chain ones ( $R = Hx \text{ and } Dc$ ) do this reluctantly, forming films on the surface of the suspension and the walls of a glass flask. This fact can be explained by poor hydratability of low-polar organic components. However, ultrasonic treatment of the alkaline and protonated niobates is not accompanied by the formation of films. Their suspensions show good sedimentation stability during photocatalytic measurements, but the actual volume concentration of such suspensions is low. In the case of the alkaline niobate with Pt nanoparticles, the suspension concentration is already quite small at the beginning of photocatalytic experiment ( $c_1$ ), which can be caused by large particles of the oxide and precipitation upon the Pt introduction. In the case of the inorganic–organic hybrids, the actual suspension concentrations increase with chain lengthening. In addition, in the case of bare oxide, suspensions precipitate during the experiment despite intense stirring ( $c_1 > c_2$ ). For Pt-loaded samples, the concentrations  $c_1$  and  $c_2$ , as a rule, stay approximately equal, which indicates the stabilization of suspensions upon the introduction of Pt (Supporting Information S6).

In addition to the stability of the reaction suspensions to sedimentation, the issue of possible exfoliation of layered compounds into nanosheets in the course of the experiments is of great importance. The appearance of nanosheets can lead to a significant increase in

the photocatalytic activity, since they have a small thickness and a large specific surface area. However, according to the data obtained (Supporting Information S5), there are practically no laminated particles in the reaction suspensions of the hybrids considered ( $c_3 < 2$  mg/L). This suggests that the inorganic–organic hybrids based on the niobate under consideration are resistant to splitting into nanosheets under the conditions of the photocatalytic experiments (at least, in the absence of bulky bases such as tetrabutylammonium hydroxide TBAOH in the solution). However, the  $c_3$  concentration is the highest for the ethoxy hybrid. Based on this, it can be assumed that its suspension contained the largest amount of a finely dispersed phase (including perovskite nanolayers) before the centrifugation.

### 2.5. Analysis of the Hybrid Inorganic–Organic Niobates after the Photocatalytic Experiment

Despite the fact that the most of the *n*-alkoxy derivatives were found to preserve their activity throughout the whole measurement time, we have analyzed some of the samples after the photocatalytic experiment (Supporting Information S7–S10). In particular, the stability under photocatalytic conditions was studied for the Pt-loaded ethoxy compound (as the most active one) as well as for methoxy and *n*-decoxy samples (as representatives with the shortest and the longest organic chain, respectively).

The XRD pattern of the ethoxy derivative taken after the photocatalytic experiment does not show any reflections from the initial inorganic–organic structure but shows all the reflections from the protonated niobate. Apparently, the organic component of the ethoxy derivative completely decomposes, and the sample turns into the initial protonated niobate. The degradation observed can be explained by the interaction of the interlayer ethoxy groups with water (hydrolysis) and photocatalytic oxidation by holes or highly reactive hydroxyl radicals, which is followed by the washout of organic residues from the interlayer space. Raman spectra and thermogravimetric curves also confirm the absence of the organic component in the final sample.

The XRD pattern of the methoxy derivative after photocatalysis does not coincide with that of the protonated niobate. However, the former is characterized by a strongly reduced interlayer distance ( $d = 14.5$  Å), which points at the probable decomposition of methoxy groups or dehydration. The Raman spectrum of the sample demonstrates extremely weak bands of the organic component. This fact is in good consistency with the results of elemental CHN-analysis and TG, indicating the retention in the interlayer space of no more than 0.35 methoxy groups per structural unit. The *n*-decoxy derivative also undergoes structural changes in the course of the photocatalytic experiment, although its Raman spectrum shows pronounced bands relating to the interlayer organic component. The final sample contains approximately 0.2 *n*-decoxy groups per formula unit.

Comparing SEM images of the samples before and after the photocatalytic experiment with platinumization, we can conclude that there are no significant changes in the morphology of the samples. Photodeposited platinum nanoparticles are observed at the SEM images as light dots with linear sizes of 6–7 nm.

Thus, many *n*-alkoxy derivatives in question turned out to be less stable under the conditions of photocatalytic hydrogen generation in comparison with earlier studied *n*-alkylamine ones [86]. However, despite the instability, most of them (including ethoxy one) preserve high activity throughout the whole measurement time, whose value cannot be explained just by hydrogen generation from the interlayer *n*-alkoxy groups even if it takes place.

### 2.6. Possible Explanations of Photocatalytic Properties of the Hybrid Inorganic–Organic Niobates

Taking into account the low stability under the photocatalytic conditions of most of the inorganic–organic compounds studied, the correct interpretation of the activity differences between samples appears to be quite problematic. In any case, special attention should be paid to the fact that their photocatalytic activity stably maintains during the experiment, suggesting that at least at initial stages, the nature of the organic component plays a significant role. The quantum efficiency of hydrogen generation clearly correlates with the

specific surface area of the samples, which, in turn, correlates with the size of the alkyl chain of the grafted *n*-alcohol. However, the specific surface appears not to be the main reason for the superior activity of the hybrids, which also correlates with the hydration degree of the interlayer space. For instance, the most active ethoxy derivative contains the highest amount of intercalated water, which could point to the significant role of the latter in the photocatalytic process. Taking both factors into account, the multiple increase in the hydrogen generation rate when going from the protonated niobate to hybrid inorganic–organic compounds may be due to the greater accessibility of their interlayer space for reactants (water and methanol), since this space is considered a separate reaction zone in heterogeneous photocatalysis being different from the external surface of the particles [42]. It is possible that the introduced organic modifiers create channels for the entrance of reactants and the removal of products that are inactive in the initial niobate. Despite the partial or even complete destruction of the organic component, these channels appear to be preserved, which explains the stable rate of hydrogen generation. However, as it was shown for the most active  $\text{HCN}_3 \times \text{EtOH}/\text{Pt}$  compound, its high activity at the final stages of the photocatalytic experiment could be associated with the sample not including any significant amounts of the organic component at all. Thus, the activity preservation should be caused by other structural or morphology factors. One of the possible explanations can be the selective reduction of platinum nanoparticles in those areas of the sample where it does not occur in the absence of an organic modifier. In particular, the increased availability of the interlayer space can lead to the formation of a nanostructured catalyst with platinum particles deposited on interlayer active sites as a final product, which can explain the persistent increased activity even after the complete decomposition of organic matter. Anyway, more research data are needed to make confident assumptions.

### 3. Materials and Methods

#### 3.1. Synthesis of the Initial Protonated Niobate

The alkaline layered perovskite-like niobate  $\text{KCa}_2\text{Nb}_3\text{O}_{10}$  ( $\text{KCN}_3$ ) was prepared according to the conventional ceramic method using preliminarily calcined  $\text{Nb}_2\text{O}_5$ ,  $\text{CaO}$ , and  $\text{K}_2\text{CO}_3$  as starting substances. The oxides were taken in stoichiometric amounts: potassium carbonate with a 30% excess to compensate for the loss during calcination. All the compounds were mixed, loaded into a grinding bowl with silicon nitride balls, and ground under an *n*-heptane layer in a Fritsch Pulverisette 7 planetary micro mill at a rotation speed of 600 rpm using a program of 10 repetitions of 10 min each separated by 5 min intervals. The mixture obtained was dried and pelletized into  $\approx 2$  g tablets at pressure of 50 bar using an Omec PI 88.00 hydraulic press. The tablets were placed into corundum crucibles with caps and calcined at 800 °C for 12 h in a Nabertherm L-011K2RN muffle furnace. Afterwards, the tablets were ground, pelletized again, calcined at 1100 °C for 24 h and, after cooling down, pulverized in an agate mortar.

To prepare the protonated niobate  $\text{HCa}_2\text{Nb}_3\text{O}_{10} \cdot 1.5\text{H}_2\text{O}$  ( $\text{HCN}_3 \cdot y\text{H}_2\text{O}$ ), which was further used as a precursor for the synthesis of *n*-alkoxy derivatives, a powder of  $\text{KCN}_3$  was treated with 12 M nitric acid at a ratio of 100 mL per 5 g of the niobate at room temperature for 1 d. After this, the product was centrifuged, thoroughly rinsed with water to remove acid residues, and dried under ambient pressure. To avoid dehydration,  $\text{HCN}_3 \cdot y\text{H}_2\text{O}$  was further stored in an atmosphere of humid air.

#### 3.2. Synthesis of *n*-Alkoxy Derivatives

Preparation of *n*-alkoxy derivatives, conventionally designated as  $\text{HCN}_3 \times \text{ROH}$  ( $\text{R}$  = methyl Me, ethyl Et, *n*-propyl Pr, *n*-butyl Bu, *n*-hexyl Hx, and *n*-decyl Dc) was performed via grafting of the corresponding *n*-alcohols into the  $\text{HCN}_3 \cdot y\text{H}_2\text{O}$  interlayer space. In each case, 1 g of the precursor was placed into a sealed PTFE vessel of a steel laboratory autoclave containing 35 mL of the *n*-alcohol or its solution. After intense shaking, the autoclave was kept at the specified temperature for 7 d. After cooling down, the solid product was filtered and rinsed with an appropriate volatile solvent to remove a residual

surface adsorbed alcohol. The detailed conditions of the *n*-alkoxy derivatives' synthesis are summarized in Table 3.

**Table 3.** Conditions for the synthesis of *n*-alkoxy derivatives  $\text{HCN}_3 \times \text{ROH}$ . In all cases, the reaction time was 7 d.

R	Precursors	Alcohol Concentration, %	Temperature, °C	Flushing	Approximate Yield, %
Me	$\text{HCN}_3 \cdot y\text{H}_2\text{O}$	90 (in water)	100	acetone	85
Et		96 (in water)			
Pr	$\text{HCN}_3 \times \text{EtOH}$	100	150	<i>n</i> -hexane	75
Bu					
Hx	$\text{HCN}_3 \times \text{PrOH}$				65
Dc					

### 3.3. Investigation of Vacuum and Hydrolytic Stability

To investigate the stability of *n*-alkoxy derivatives at reduced pressure, their samples were placed in a desiccator connected to an oil vacuum pump Edwards E2M1.5 and held under residual pressure of  $1 \times 10^{-4}$  atm for 5 d and 10 d. The compositions of the resulting samples were determined via CHN analysis.

For the study of hydrolytic stability, 0.05 g of each derivative was placed into a sealed glass tube with 10 mL of water and stirred for 1 d and 10 d. Afterwards, the solid phase was filtered and studied by X-ray diffraction analysis and Raman spectroscopy.

### 3.4. Investigation of Photocatalytic Activity

Photocatalytic activity was studied with regard to the light-driven hydrogen generation from the model 1 mol % aqueous solution of methanol both for bare samples and for their composites with Pt nanoparticles as a cocatalyst. The same measurements were also conducted for the "classic" photocatalyst  $\text{TiO}_2$  P25 Degussa taken as a reference. The hydrogen evolution rate  $\omega$ , apparent quantum efficiency  $\phi$ , and multiplicity  $k_{\text{Pt}}$  of increase in the rate after Pt loading were used as quantitative indicators of photocatalytic activity.

The measurements were performed on a laboratory photocatalytic setting used in our previous studies [85,86] consisting of an illuminator, photocatalytic cell additionally providing light filtration, and the reaction mixture cooling, gas chromatograph, and closed gas circulation system connecting the last two components (Supporting information S11). An arc mercury tube lamp DRT-125 (125 W) serves as an ultraviolet irradiation source. The photocatalytic cell represents an external irradiation reactor including two compartments equipped with branch pipes for the supply and removal of solutions and gases. The closest compartment to the lamp, used for light filtration, is filled with an aqueous solution of KCl and NaBr (6 g/L of each salt). The light filter allows cutting of far-ultraviolet irradiation ( $\lambda < 220$  nm) that could promote the undesirable reaction of direct methanol photolysis. The filter also provides cooling for the cell, which is achieved by its continuous circulation through a thermostat connected to the water-cooling system and maintaining a temperature of 15 °C. The compartment farthest from the lamp is for the reaction suspension, which is intensively stirred during the experiment. Gaseous reaction products come from the cell into the gas circulation system. Their detection is conducted according to a specified time program by a Shimadzu GC-2014 gas chromatograph equipped with a 30 m long Rt-Msieve 5A capillary column coated with molecular sieves as well as a thermal conductivity detector using argon as a carrier gas.

To prepare the reaction suspension, in each case, 0.03 g of the sample was placed in a round-bottom flask containing 60 mL of 1 mol % aqueous methanol. The flask was shaken, sealed, and left for 10 min. Then, the mixture was sonicated in an Elmasonic S10H bath (60 W) for 10 min. In the case of bare samples investigation, after the light filter circulation

and magnetic stirrer had been turned on, 54 mL of the suspension obtained was pumped into the reaction compartment of the cell, and irradiation and argon flushing were switched on. After 15 min, 4 mL of the suspension was taken from the cell to establish the actual volume sample concentration and the pH of the medium before the measurement beginning ( $c_1$ ,  $\text{pH}_1$ ). After 15 min, argon flushing of the cell was switched off, and the photocatalytic activity measurement, consisting of chromatographic analysis of the gaseous phase every 15 min, was conducted for 2 h. Then, the lamp was switched off, and the chromatographic analysis of the gaseous phase was continued for 45 min to prove the absence of hydrogen generation without external irradiation (dark stage). Thereafter, 4 mL of the suspension was sampled to determine the volume concentration and pH of the medium at the end of the measurement ( $c_2$ ,  $\text{pH}_2$ ). After this, 30 mL of the residual suspension was centrifuged at a separation factor  $F = 1000$  for 1 h to precipitate bulk non-exfoliated particles and determine the perovskite nanolayers' concentration in the final colloidal solution as well as its pH value ( $c_3$ ,  $\text{pH}_3$ ). In the case of platinized samples investigation, the volume of the initial suspension for loading into the reaction compartment was 53 mL. After 15 min from the lamp and argon flushing switching on, 1.1 mL of a 2.56 mM  $\text{H}_2\text{PtCl}_6$  aqueous solution was injected into the reaction suspension to perform in situ photocatalytic platinization. The solution volume was calculated to provide the mass fraction of Pt in the sample of 1%, assuming its full reduction. The gaseous phase was analyzed every 5 min. If the hydrogen evolution rate exceeded  $500 \mu\text{mol/h}$ , the photocatalytic measurement program was divided into several sections of 20–30 min, each one separated by 10 min argon flushings to reduce pressure in the system. Dark stages of 20 min each were performed both in the middle and at the end of the measurement. Other experimental conditions and procedures were the same.

### 3.5. Instrumentation

#### 3.5.1. XRD

Powder X-ray diffraction (XRD) analysis of the samples was performed on a Rigaku Miniflex II benchtop diffractometer (Tokyo, Japan) ( $\text{CuK}\alpha$  radiation, angle range  $2\theta = 3\text{--}60^\circ$ , scanning rate  $10^\circ/\text{min}$ , step  $0.02^\circ$ ). The lattice parameters were calculated on the basis of all the reflections observed using *DiffraPlus Topas V 3.0* software.

#### 3.5.2. Raman Spectroscopy

Raman scattering spectra were collected on a Bruker Senterra spectrometer (Billerica, USA) in the Raman shift range of  $100\text{--}4000 \text{ cm}^{-1}$  using the incident laser 488 nm (power 0.4–20 mW, accumulation time 10–250 s).

#### 3.5.3. NMR Spectroscopy

Carbon nuclear magnetic resonance ( $^{13}\text{C}$  NMR) spectra of the *n*-alkoxy derivatives were recorded on a Bruker Avance III 400 WB spectrometer (Billerica, USA) at an operating frequency of 100.64 MHz using tetramethylsilane as an external reference. The interpretation of the NMR spectra was based on matching the bands observed with the magnetically active nuclei of the samples ( $^{13}\text{C}$  nuclei of *n*-alkoxy groups) using reference data on chemical shifts in NMR spectroscopy.

#### 3.5.4. DRS

Diffuse reflectance spectra (DRS) were obtained on a Shimadzu UV-2550 spectrophotometer (Kyoto, Japan) with an ISR-2200 integrating sphere attachment in the range of 190–800 nm using barium sulfate as an external reference with reflection coefficient  $R = 1$ . Optical bandgap energies  $E_g$  were found via the transformation of the reflectance spectra into coordinates  $(F \cdot h\nu)^{1/2} = f(h\nu)$ , where  $F = (1 - R)^2 / 2R$  is a Kubelka–Munk function, and there is the further determination of abscissas of the intersection points of linear sections of the graphs.

### 3.5.5. CHN Analysis

Carbon content in the *n*-alkoxy derivatives was determined via the elemental CHN-analysis on a Euro EA3028-HT analyzer (Pavia, Italy).

### 3.5.6. TG

Thermogravimetric (TG) analysis was performed on a Netzsch TG 209 F1 Libra thermobalance (Selb, Germany) in a synthetic air atmosphere (100 mL/min flow). The temperature program included heating each sample from room temperature to 950 °C at a rate of 10 °C/min followed by keeping at the maximum temperature for 20 min to achieve establishing the constant mass.

### 3.5.7. SEM

Morphology of the particles was investigated on a Zeiss Merlin scanning electron microscope (SEM) (Oberkochen, Germany) equipped with a field emission cathode, electron optics column Gemini II, and oil-free vacuum system.

### 3.5.8. BET

Specific surface areas *S* were measured according to the Brunauer–Emmett–Teller (BET) method on a Micromeritics ASAP 2020MP system (Norcross, USA) with previous vacuum degassing at room temperature using N<sub>2</sub> and Kr as adsorbates.

### 3.5.9. ICP-AES

Concentrations of the perovskite nanolayers in colloidal solutions used for building spectrophotometric calibration plots were determined by inductively coupled plasma atomic emission spectroscopy (ICP-AES) on a Shimadzu ICPE-9000 spectrometer (Kyoto, Japan) after preliminary acid digestion.

### 3.5.10. Spectrophotometry

Actual volume concentrations of samples in suspensions *c*<sub>1</sub>, *c*<sub>2</sub>, and *c*<sub>3</sub> were determined via their spectrophotometric analysis performed on a Thermo Scientific Genesys 10S UV-Vis spectrophotometer (Waltham, USA) using the previously built calibration plots (Supporting information S12). The spectrophotometry was performed in the range of optical density *A* < 2. The 1 mol % aqueous methanol was used for dilution and baseline recording.

### 3.5.11. pH Measurement

The pH values of a reaction suspensions' medium were determined using a Mettler Toledo (Greifensee, Switzerland) laboratory pH meter Toledo SevenCompact S220 equipped with an InLab Expert Pro-ISM electrode.

## 4. Conclusions

In this study, we have comprehensively investigated a number of *n*-alkoxy derivatives of the layered niobate HCa<sub>2</sub>Nb<sub>3</sub>O<sub>10</sub> and their photocatalytic activity for hydrogen production. All the hybrids without exceptions were found to be superior in photocatalytic activity to the initial niobate, both bare and with the addition of Pt as a cocatalyst. The photocatalytic activity correlates well with the amount of interlayer water in the hybrids as well as with their specific surface area. The organic modification turned out to be an effective way to increase the photocatalytic activity of the niobates toward light-driven hydrogen generation from aqueous methanol. The series of *n*-alkoxy hybrids showed greater activity compared to that of the *n*-alkylamine ones investigated earlier, which makes the study of the former a more promising direction for research. In the absence of a cocatalyst, the introduction of organic modifiers into the interlayer space provided an increase in the activity by more than 10 times in comparison with that of the initial unmodified protonated niobate. Unfortunately, most of the hybrid samples turned out to be unstable under photo-

catalytic conditions, and some of them experienced practically complete degradation of the organic component by the end of the experiment. Nevertheless, these changes were not accompanied by a noticeable photocatalytic activity reduction. Further studies in this field may be focused on searching for other organic modifiers (other than primary amines and alcohols) that are more stable under photocatalytic conditions and provide an expansion of the light absorption to the visible region.

**Supplementary Materials:** The following are available online at <https://www.mdpi.com/article/10.3390/catal11080897/s1>, S1: Diffuse reflectance spectra and Tauc plots for initial niobates and their *n*-alkoxy derivatives, S2: Quantitative compositions *n*-alkoxy derivatives before and after keeping under reduced pressure, S3: XRD patterns of *n*-alkoxy derivatives before and after water treatment, S4: Raman spectra of *n*-alkoxy derivatives before and after water treatment, S5: Actual volume concentrations and pH values of reaction suspensions, S6: Comparison of actual concentrations of photocatalysts in the reaction suspensions in the beginning and in the ending of photocatalytic measurements, S7: XRD patterns of some *n*-alkoxy derivatives before and after photocatalytic (PC) experiments, S8: Raman spectra of some *n*-alkoxy derivatives before and after photocatalytic (PC) experiments, S9: TG curves of some *n*-alkoxy derivatives before and after photocatalytic (PC) experiments, S10: SEM images of some *n*-alkoxy derivatives before and after photocatalytic (PC) experiments, S11: Scheme of (a) photocatalytic setting and (b) reaction cell, S12: Spectrophotometric calibrations for express measurement of photocatalytic suspensions' concentrations.

**Author Contributions:** Conceptualization, O.I.S., I.A.Z., methodology, O.I.S. and I.A.R.; investigation, V.V.V., S.A.K., A.N.B., E.N.M. and I.A.M.; data curation, O.I.S.; writing—original draft preparation, V.V.V. and S.A.K.; writing—review and editing, O.I.S., I.A.Z. and I.A.R.; visualization, O.I.S. and V.V.V.; supervision, I.A.Z.; funding acquisition, O.I.S. and I.A.Z. All authors have read and agreed to the published version of the manuscript.

**Funding:** The study was financially supported by Russian Science Foundation (synthesis of hybrid compounds, as well as study of their properties was carried out within the framework of the project 20-73-00027; study of photocatalytic activity, as well as surface area, bandgap energies and compounds' stability was carried out within the framework of the project 19-13-00184).

**Data Availability Statement:** The data presented in this study are available in the article.

**Acknowledgments:** The study was conducted using the equipment of the Saint Petersburg State University Research Park: Center for X-ray Diffraction Studies, Center for Optical and Laser Research, Center for Magnetic Resonance, Center for Chemical Analysis and Materials Research, Center for Thermal Analysis and Calorimetry, Interdisciplinary Center for Nanotechnology, Center for Innovative Technologies of Composite Nanomaterials.

**Conflicts of Interest:** The authors declare no conflict of interest.

## References

1. Moiseev, I.I. Green chemistry: Development trajectory. *Russ. Chem. Rev.* **2013**, *82*, 616–623. [[CrossRef](#)]
2. Kozlova, E.A.; Parmon, V.N. Heterogeneous semiconductor photocatalysts for hydrogen production from aqueous solutions of electron donors. *Russ. Chem. Rev.* **2017**, *86*, 870–906. [[CrossRef](#)]
3. Nikolaidis, P.; Poullikkas, A. A comparative overview of hydrogen production processes. *Renew. Sustain. Energy Rev.* **2017**, *67*, 597–611. [[CrossRef](#)]
4. Ismail, A.A.; Bahnemann, D.W. Photochemical splitting of water for hydrogen production by photocatalysis: A review. *Sol. Energy Mater. Sol. Cells* **2014**, *128*, 85–101. [[CrossRef](#)]
5. Ahmad, H.; Kamarudin, S.K.; Minggu, L.J.; Kassim, M. Hydrogen from photo-catalytic water splitting process: A review. *Renew. Sustain. Energy Rev.* **2015**, *43*, 599–610. [[CrossRef](#)]
6. Takane, K. Photocatalytic Water Splitting: Quantitative Approaches toward Photocatalyst by Design. *ACS Catal.* **2017**, *7*, 8006–8022. [[CrossRef](#)]
7. Walter, M.G.; Warren, E.L.; McKone, J.R.; Boettcher, S.W.; Mi, Q.; Santori, E.A.; Lewis, N.S. Solar water splitting cells. *Chem. Rev.* **2010**, *110*, 6446–6473. [[CrossRef](#)] [[PubMed](#)]
8. Rozhkova, E.; Ariga, K. *From Molecules to Materials Pathways to Artificial Photosynthesis*; Springer: Berlin/Heidelberg, Germany, 2015.
9. Christoforidis, K.C.; Fornasiero, P. Photocatalytic Hydrogen Production: A Rift into the Future Energy Supply. *ChemCatChem* **2017**, *9*, 1523–1544. [[CrossRef](#)]

10. Puga, A.V. Photocatalytic production of hydrogen from biomass-derived feedstocks. *Coord. Chem. Rev.* **2016**, *315*, 1–66. [CrossRef]
11. Liu, R.; Yoshida, H.; ichiro Fujita, S.; Arai, M. Photocatalytic hydrogen production from glycerol and water with NiOx/TiO<sub>2</sub> catalysts. *Appl. Catal. B Environ.* **2014**, *144*, 41–45. [CrossRef]
12. Taboada, E.; Angurell, I.; Llorca, J. Hydrogen photoproduction from bio-derived alcohols in an optical fiber honeycomb reactor loaded with Au/TiO<sub>2</sub>. *J. Photochem. Photobiol. A Chem.* **2014**, *281*, 35–39. [CrossRef]
13. Al-Azri, Z.H.N.; Chen, W.T.; Chan, A.; Jovic, V.; Ina, T.; Idriss, H.; Waterhouse, G.I.N. The roles of metal co-catalysts and reaction media in photocatalytic hydrogen production: Performance evaluation of M/TiO<sub>2</sub> photocatalysts (M = Pd, Pt, Au) in different alcohol-water mixtures. *J. Catal.* **2015**, *329*, 355–367. [CrossRef]
14. Dosado, A.G.; Chen, W.T.; Chan, A.; Sun-Waterhouse, D.; Waterhouse, G.I.N. Novel Au/TiO<sub>2</sub> photocatalysts for hydrogen production in alcohol-water mixtures based on hydrogen titanate nanotube precursors. *J. Catal.* **2015**, *330*, 238–254. [CrossRef]
15. Wang, X.; Dong, H.; Hu, Z.; Qi, Z.; Li, L. Fabrication of a Cu<sub>2</sub>O/Au/TiO<sub>2</sub> composite film for efficient photocatalytic hydrogen production from aqueous solution of methanol and glucose. *Mater. Sci. Eng. B Solid-State Mater. Adv. Technol.* **2017**, *219*, 10–19. [CrossRef]
16. Li, C.; Wang, H.; Ming, J.; Liu, M.; Fang, P. Hydrogen generation by photocatalytic reforming of glucose with heterostructured CdS/MoS<sub>2</sub> composites under visible light irradiation. *Int. J. Hydrogen Energy* **2017**, *42*, 16968–16978. [CrossRef]
17. Jaswal, R.; Shende, R.; Nan, W.; Shende, A. Photocatalytic reforming of pinewood (*Pinus ponderosa*) acid hydrolysate for hydrogen generation. *Int. J. Hydrogen Energy* **2017**, *42*, 2839–2848. [CrossRef]
18. Udom, I.; Myers, P.; Ram, M.K.; Hepp, A.F.; Archibong, E.; Stefanakos, E.K.; Goswami, D.Y. Optimization of Photocatalytic Degradation of Phenol Using Simple Photocatalytic Reactor. *Am. J. Anal. Chem.* **2014**, *5*, 743–750. [CrossRef]
19. Long, Z.; Li, Q.; Wei, T.; Zhang, G.; Ren, Z. Historical development and prospects of photocatalysts for pollutant removal in water. *J. Hazard. Mater.* **2020**, *395*, 122599. [CrossRef]
20. Rueda-Marquez, J.J.; Levchuk, I.; Fernandez-Ibañez, P.; Sillanpää, M. A critical review on application of photocatalysis for toxicity reduction of real wastewaters. *J. Clean. Prod.* **2020**, *258*, 120694. [CrossRef]
21. Zhang, G.; Zhang, X.; Meng, Y.; Pan, G.; Ni, Z.; Xia, S. Layered double hydroxides-based photocatalysts and visible-light driven photodegradation of organic pollutants: A review. *Chem. Eng. J.* **2020**, *392*, 123684. [CrossRef]
22. Karthikeyan, C.; Arunachalam, P.; Ramachandran, K.; Al-Mayouf, A.M.; Karuppuchamy, S. Recent advances in semiconductor metal oxides with enhanced methods for solar photocatalytic applications. *J. Alloys Compd.* **2020**, *828*, 154281. [CrossRef]
23. Teixeira, I.; Quiroz, J.; Homsí, M.; Camargo, P. An overview of the photocatalytic H<sub>2</sub> evolution by semiconductor-based materials for nonspecialists. *J. Braz. Chem. Soc.* **2020**, *31*, 211–229. [CrossRef]
24. Schaak, R.E.; Mallouk, T. Perovskites by Design: A Toolbox of Solid-State Reactions. *Chem. Mater.* **2002**, *14*, 1455–1471. [CrossRef]
25. Uppuluri, R.; Gupta, A.S.; Rosas, A.S.; Mallouk, T.E. Soft chemistry of ion-exchangeable layered metal oxides. *Chem. Soc. Rev.* **2018**, *47*, 2401–2430. [CrossRef]
26. Tani, S.; Komori, Y.; Hayashi, S.; Sugahara, Y. Local environments and dynamics of hydrogen atoms in protonated forms of ion-exchangeable layered perovskites estimated by solid-state <sup>1</sup>H NMR. *J. Solid State Chem.* **2006**, *179*, 3357–3364. [CrossRef]
27. Utkina, T.; Chislov, M.; Silyukov, O.; Burovikhina, A.; Zvereva, I.A. TG and DSC investigation of water intercalation and protonation processes in perovskite-like layered structure of titanate K<sub>2</sub>Nd<sub>2</sub>Ti<sub>3</sub>O<sub>10</sub>. *J. Therm. Anal. Calorim.* **2016**, *125*, 281–287. [CrossRef]
28. Silyukov, O.; Chislov, M.; Burovikhina, A.; Utkina, T.; Zvereva, I. Thermogravimetry study of ion exchange and hydration in layered oxide materials. *J. Therm. Anal. Calorim.* **2012**, *110*, 187–192. [CrossRef]
29. Jacobson, A.; Lewandowski, J.; Johnson, J.W. Ion exchange of the layered perovskite KCa<sub>2</sub>Nb<sub>3</sub>O<sub>10</sub> by protons. *J. Less Common Met.* **1986**, *116*, 137–146. [CrossRef]
30. Kumada, N.; Fukazawa, Y.; Yonesaki, Y.; Takei, T.; Kinomura, N. Ion-exchange Reaction of Protonated Layer Compounds with Bi<sup>3+</sup> Ion. *Clay Sci.* **2006**, *12*, 331–335. Available online: [https://www.jstage.jst.go.jp/article/jcssjclayscience1960/12/Supplement2/12\\_Supplement2\\_331/\\_pdf/-char/ja](https://www.jstage.jst.go.jp/article/jcssjclayscience1960/12/Supplement2/12_Supplement2_331/_pdf/-char/ja) (accessed on 1 June 2021).
31. Zvereva, I.A.; Silyukov, O.; Chislov, M. Ion-exchange reactions in the structure of perovskite-like layered oxides: I. Protonation of NaNdTiO<sub>4</sub> complex oxide. *Russ. J. Gen. Chem.* **2011**, *81*, 1434–1441. [CrossRef]
32. Yip, T.W.S.; Cussen, E.J. Ion Exchange and Structural Aging in the Layered Perovskite Phases. *Inorg. Chem.* **2013**, *52*, 6985–6993. [CrossRef]
33. Yafarova, L.V.; Silyukov, O.I.; Myshkovskaya, T.D.; Minich, I.A.; Zvereva, I.A. New data on protonation and hydration of perovskite-type layered oxide KCa<sub>2</sub>Nb<sub>3</sub>O<sub>10</sub>. *J. Therm. Anal. Calorim.* **2020**, *1*, 87–93. [CrossRef]
34. Silyukov, O.I.; Minich, I.A.; Zvereva, I.A. Synthesis of Protonated Derivatives of Layered Perovskite-Like Bismuth Titanates. *Glass Phys. Chem.* **2018**, *44*, 115–119. [CrossRef]
35. Rodionov, I.A.; Silyukov, O.I.; Utkina, T.D.; Chislov, M.V.; Sokolova, Y.P.; Zvereva, I.A. Photocatalytic properties and hydration of perovskite-type layered titanates A<sub>2</sub>Ln<sub>2</sub>Ti<sub>3</sub>O<sub>10</sub> (A = Li, Na, K; Ln = La, Nd). *Russ. J. Gen. Chem.* **2012**, *82*, 1191–1196. [CrossRef]
36. Kurnosenko, S.A.; Silyukov, O.I.; Zvereva, I.A. Preparation of Porous Particles of Layered Perovskite-Like Titanate HLaTiO<sub>4</sub>. *Glass Phys. Chem.* **2020**, *46*, 272–276. [CrossRef]
37. Cattaneo, A.S.; Ferrara, C.; Marculescu, A.M.; Giannici, F.; Tealdi, C.; Martorana, A.; Mustarelli, P. Solid-state NMR characterization of the structure and thermal stability of hybrid organic–inorganic compounds based on a HLaNb<sub>2</sub>O<sub>7</sub> Dion–Jacobson layered perovskite. *Phys. Chem. Chem. Phys.* **2016**, *18*, 21903–21912. [CrossRef]

38. Wang, B.; Dong, X.; Pan, Q.; Cheng, Z.; Yang, Y. Intercalation behavior of n-alkylamines into an A-site defective layered perovskite  $H_2W_2O_7$ . *J. Solid State Chem.* **2007**, *180*, 1125–1129. [[CrossRef](#)]
39. Jacobson, A.J.; Johnson, J.W.; Lewandowski, J. Intercalation of the layered solid acid  $HCa_2Nb_3O_{10}$  by organic amines. *Mater. Res. Bull.* **1987**, *22*, 45–51. [[CrossRef](#)]
40. Takata, T.; Furumi, Y.; Shinohara, K.; Tanaka, A.; Hara, M.; Kondo, J.; Domen, K. Photocatalytic Decomposition of Water on Spontaneously Hydrated Layered Perovskites. *Chem. Mater.* **1997**, *9*, 1063–1064. [[CrossRef](#)]
41. Rodionov, I.A.; Zvereva, I.A. Photocatalytic activity of layered perovskite-like oxides in practically valuable chemical reactions. *Russ. Chem. Rev.* **2016**, *85*, 248–279. [[CrossRef](#)]
42. Cui, W.; Liu, L.; Ma, S.; Liang, Y.; Zhang, Z. CdS-sensitized  $K_2La_2Ti_3O_{10}$  composite: A new photocatalyst for hydrogen evolution under visible light irradiation. *Catal. Today* **2013**, *207*, 44–49. [[CrossRef](#)]
43. Cui, W.; Liu, L.; Ma, S.; Liang, Y.; Zhang, Z. Substitution effects of  $In^{3+}$  by  $Fe^{3+}$  on photocatalytic and structural properties of  $Bi_2InNbO_7$  photocatalysts. *J. Mol. Catal.* **2001**, *168*, 289–297.
44. Reddy, V.; Hwang, D.; Lee, J. Effect of Zr substitution for Ti in  $KLaTiO_4$  for photocatalytic water splitting. *Catal. Lett.* **2003**, *90*, 39–44. [[CrossRef](#)]
45. Kumar, V.; Govind, Uma, S. Investigation of cation ( $Sn^{2+}$ ) and anion ( $N_3^-$ ) substitution in favor of visible light photocatalytic activity in the layered perovskite  $K_2La_2Ti_3O_{10}$ . *J. Hazard. Mater.* **2011**, *189*, 502–508. [[CrossRef](#)] [[PubMed](#)]
46. Zhou, Y.; Wen, T.; Guo, Y.; Yang, B.; Wang, Y. Controllable doping of nitrogen and tetravalent niobium affords yellow and black calcium niobate nanosheets for enhanced photocatalytic hydrogen evolution. *RSC Adv.* **2016**, *6*, 64930–64936. [[CrossRef](#)]
47. Kawashima, K.; Hojamberdiev, M.; Chen, S.; Yubuta, K.; Wagata, H.; Domen, K.; Teshima, K. Understanding the effect of partial  $N_3^-$ -to- $O_2^-$  substitution and  $H^+$ -to- $K^+$  exchange on photocatalytic water reduction activity of Ruddlesden–Popper layered perovskite  $KLaTiO_4$ . *Mol. Catal.* **2017**, *432*, 250–258. [[CrossRef](#)]
48. Huang, Y.; Li, J.; Wei, Y.; Li, Y.; Lin, J.; Wu, J. Fabrication and photocatalytic property of Pt-intercalated layered perovskite niobates  $H_{1-x}LaNb_{2-x}MoxO_7$  ( $x = 0-0.15$ ). *J. Hazard. Mater.* **2009**, *166*, 103–108. [[CrossRef](#)]
49. Huang, Y.; Li, Y.; Wei, Y.; Huang, M.; Wu, J. Photocatalytic property of partially substituted Pt-intercalated layered perovskite,  $ASr_2TaxNb_{3-x}O_{10}$  ( $A = K, H; x = 0, 1, 1.5, 2$  and  $3$ ). *Sol. Energy Mater. Sol. Cells* **2011**, *95*, 1019–1027. [[CrossRef](#)]
50. Oshima, T.; Wang, Y.; Lu, D.; Yokoi, T.; Maeda, K. Photocatalytic overall water splitting on Pt nanocluster-intercalated, restacked  $KCa_2Nb_3O_{10}$  nanosheets: The promotional effect of co-existing ions. *Nanoscale Adv.* **2019**, *1*, 189–194. [[CrossRef](#)]
51. Cui, W.; Qi, Y.; Liu, L.; Rana, D.; Hu, J.; Liang, Y. Synthesis of  $PbS-K_2La_2Ti_3O_{10}$  composite and its photocatalytic activity for hydrogen production. *Prog. Nat. Sci. Mater. Int.* **2012**, *22*, 120–125. [[CrossRef](#)]
52. Cui, W.; Guo, D.; Liu, L.; Hu, J.; Rana, D.; Liang, Y. Preparation of  $ZnIn_2S_4/K_2La_2Ti_3O_{10}$  composites and their photocatalytic  $H_2$  evolution from aqueous  $Na_2S/Na_2SO_3$  under visible light irradiation. *Catal. Commun.* **2014**, *48*, 55–59. [[CrossRef](#)]
53. Saito, K.; Kozeni, M.; Sohmiya, M.; Komaguchi, K.; Ogawa, M.; Sugahara, Y.; Ide, Y. Unprecedentedly enhanced solar photocatalytic activity of a layered titanate simply integrated with  $TiO_2$  nanoparticles. *Phys. Chem. Chem. Phys.* **2016**, *18*, 30920–30925. [[CrossRef](#)]
54. Liu, Y.; Zhou, Y.; Lv, C.; Zhang, C.; Jin, X.; Meng, Q.; Chen, G. Construction of 2D-composite  $HCa_2Nb_3O_{10}/CaNb_2O_6$  heterostructured photocatalysts with enhanced hydrogen production performance. *New J. Chem.* **2018**, *42*, 681–687. [[CrossRef](#)]
55. Chen, X.; Shen, S.; Guo, L.; Mao, S. Semiconductor-based photocatalytic hydrogen generation. *Chem. Rev.* **2010**, *110*, 6503–6570. [[CrossRef](#)] [[PubMed](#)]
56. Zhang, L.; Wong, K.-H.; Chen, Z.; Yu, J.; Zhao, J.; Hu, C.; Chan, C.-Y.; Wong, P.-K. AgBr-Ag- $Bi_2WO_6$  nanojunction system: A novel and efficient photocatalyst with double visible-light active components. *Appl. Catal. A Gen.* **2009**, *363*, 221–229. [[CrossRef](#)]
57. Kim, H.G.; Jeong, E.D.; Borse, P.H.; Jeon, S.; Yong, K.; Lee, J.S.; Li, W.; Oh, S.H. Photocatalytic Ohmic layered nanocomposite for efficient utilization of visible light photons. *Appl. Phys. Lett.* **2006**, *89*, 2012–2015. [[CrossRef](#)]
58. Kim, H.G.; Borse, P.H.; Choi, W.; Lee, J.S. Photocatalytic Nanodiodes for Visible-Light Photocatalysis. *Angew. Chem.* **2005**, *117*, 4661–4665. [[CrossRef](#)]
59. Zhang, L.; Wang, G.; Xiong, Z.; Tang, H.; Jiang, C. Fabrication of flower-like direct Z-scheme  $\beta-Bi_2O_3/g-C_3N_4$  photocatalyst with enhanced visible light photoactivity for Rhodamine B degradation. *Appl. Surf. Sci.* **2018**, *436*, 162–171. [[CrossRef](#)]
60. Youngblood, W.J.; Lee, S.-H.A.; Maeda, K.; Mallouk, T. Visible light water splitting using dye-sensitized oxide semiconductors. *Acc. Chem. Res.* **2009**, *42*, 1966–1973. [[CrossRef](#)] [[PubMed](#)]
61. Hu, B.; Cai, F.; Chen, T.; Fan, M.; Song, C.; Yan, X.; Shi, W. Enhanced Photocatalytic Activity for Hydrogen Production under Visible Light Irradiation. *ACS Appl. Mater. Interfaces* **2015**, *7*, 33. [[CrossRef](#)]
62. Gao, Y.; Lin, J.; Zhang, Q.; Yu, H.; Ding, F.; Xu, B.; Sun, Y.; Xu, Z. Facile synthesis of heterostructured  $YVO_4/g-C_3N_4/Ag$  photocatalysts with enhanced visible-light photocatalytic performance. *Appl. Catal. B Environ.* **2018**, *224*, 586–593. [[CrossRef](#)]
63. Cui, Z.; Yang, H.; Zhao, X. Enhanced photocatalytic performance of  $g-C_3N_4/Bi_4Ti_3O_{12}$  heterojunction nanocomposites. *Mater. Sci. Eng. B Solid-State Mater. Adv. Technol.* **2018**, *229*, 160–172. [[CrossRef](#)]
64. Guo, Y.; Li, J.; Gao, Z.; Zhu, X.; Liu, Y.; Wei, Z.; Zhao, W.; Sun, C. A simple and effective method for fabricating novel p-n heterojunction photocatalyst  $g-C_3N_4/Bi_4Ti_3O_{12}$  and its photocatalytic performances. *Appl. Catal. B Environ.* **2016**, *192*, 57–71. [[CrossRef](#)]
65. Maeda, K.; Mallouk, T.E. Two-Dimensional Metal Oxide Nanosheets as Building Blocks for Artificial Photosynthetic Assemblies. *Bull. Chem. Soc. Jpn.* **2018**, *92*, 38–54. [[CrossRef](#)]

66. Gómez-Romero, P.; Sanchez, C. *Functional Hybrid Materials*; Wiley-VCH Verlag GmbH & Co. KGaA: Weinheim, Germany, 2006.
67. Sanchez, C.; Soler-Illia, G.; Ribot, F.; Lalot, T.; Mayer, C.R.; Cabuil, V. Designed hybrid organic-inorganic nanocomposites from functional nanobuilding blocks. *Chem. Mater.* **2001**, *13*, 3061–3083. [[CrossRef](#)]
68. Mir, S.H.; Nagahara, L.A.; Thundat, T.; Tabari, P.M.; Furukawa, H.; Khosla, A. Review—Organic-Inorganic Hybrid Functional Materials: An Integrated Platform for Applied Technologies. *J. Electrochem. Soc.* **2018**, *165*, B3137–B3156. [[CrossRef](#)]
69. Tahara, S.; Ichikawa, T.; Kajiwara, G.; Sugahara, Y. Reactivity of the Ruddlesden–Popper Phase  $\text{H}_2\text{La}_2\text{Ti}_3\text{O}_{10}$  with Organic Compounds: Intercalation and Grafting Reactions. *Chem. Mater.* **2007**, *19*, 2352–2358. [[CrossRef](#)]
70. Silyukov, O.I.; Kurnosenko, S.A.; Zvereva, I.A. Intercalation of Methylamine into the Protonated Forms of Layered Perovskite-Like Oxides  $\text{HLnTiO}_4$  (Ln = La and Nd). *Glass Phys. Chem.* **2018**, *44*, 428–432. [[CrossRef](#)]
71. Minich, I.A.; Silyukov, O.I.; Gak, V.V.; Borisov, E.V.; Zvereva, I.A. Synthesis of Organic-Inorganic Hybrids Based on Perovskite-like Bismuth Titanate  $\text{H}_2\text{K}_{0.5}\text{Bi}_{2.5}\text{Ti}_4\text{O}_{13}\cdot\text{H}_2\text{O}$  and n-Alkylamines. *ACS Omega* **2020**, *5*, 8158–8168. [[CrossRef](#)]
72. Kurnosenko, S.A.; Silyukov, O.I.; Minich, I.A.; Zvereva, I.A. Exfoliation of methylamine and n-butylamine derivatives of layered perovskite-like oxides  $\text{HLnTiO}_4$  and  $\text{H}_2\text{Ln}_2\text{Ti}_3\text{O}_{10}$  (Ln = La, Nd) into nanolayers. *Glass Phys. Chem.* **2021**, *44*, 428–432.
73. Kurnosenko, S.A.; Silyukov, O.I.; Mazur, A.S.; Zvereva, I.A. Synthesis and thermal stability of new inorganic-organic perovskite-like hybrids based on layered titanates  $\text{HLnTiO}_4$  (Ln = La, Nd). *Ceram. Int.* **2019**, *46*, 5058–5068. [[CrossRef](#)]
74. Silyukov, O.I.; Khramova, A.D.; Zvereva, I.A. Synthesis of Organic-Inorganic Derivatives of Perovskite-Like Layered  $\text{HCa}_2\text{Nb}_3\text{O}_{10}$  Oxide with Monoethanolamine and Glycine. *Glass Phys. Chem.* **2020**, *46*, 256–259. [[CrossRef](#)]
75. Han, Y.-S.; Park, I.; Choy, J.-H. Exfoliation of layered perovskite,  $\text{KCa}_2\text{Nb}_3\text{O}_{10}$ , into colloidal nanosheets by a novel chemical process. *J. Mater. Chem.* **2001**, *11*, 1277–1282. [[CrossRef](#)]
76. Tahara, S.; Sugahara, Y. Interlayer Surface Modification of the Protonated Triple-Layered Perovskite  $\text{HCa}_2\text{Nb}_3\text{O}_{10}\cdot x\text{H}_2\text{O}$  with n-Alcohols. *Langmuir* **2003**, *19*, 9473–9478. [[CrossRef](#)]
77. Shelyapina, M.G.; Lushpinskaya, I.P.; Kurnosenko, S.A.; Silyukov, O.I.; Zvereva, I.A. Identification of Intercalates and Grafted Organic Derivatives of  $\text{H}_2\text{La}_2\text{Ti}_3\text{O}_{10}$  by Multinuclear NMR. *Russ. J. Gen. Chem.* **2020**, *90*, 760–761. [[CrossRef](#)]
78. Shelyapina, M.G.; Silyukov, O.I.; Lushpinskaya, I.P.; Kurnosenko, S.A.; Mazur, A.S.; Shenderovich, I.G.; Zvereva, I.A. NMR Study of Intercalates and Grafted Organic Derivatives of  $\text{H}_2\text{La}_2\text{Ti}_3\text{O}_{10}$ . *Molecules* **2020**, *25*, 5229. [[CrossRef](#)] [[PubMed](#)]
79. Minich, I.A.; Silyukov, O.I.; Mazur, A.S.; Zvereva, I.A. Grafting reactions of perovskite-like bismuth titanate  $\text{H}_2\text{K}_{0.5}\text{Bi}_{2.5}\text{Ti}_4\text{O}_{13}\cdot\text{H}_2\text{O}$  with n-alcohols. *Ceram. Int.* **2020**, *46*, 29373–29381. [[CrossRef](#)]
80. Wang, C.; Tang, K.; Wang, D.; Liu, Z.; Wang, L.; Zhu, Y.; Qian, Y. A new carbon intercalated compound of Dion-Jacobson phase  $\text{HLaNb}_2\text{O}_7$ . *J. Mater. Chem.* **2012**, *22*, 11086–11092. [[CrossRef](#)]
81. Aznar, A.J.; Sanz, J.; Ruiz-Hitzky, E. Mechanism of the grafting of organosilanes on mineral surfaces. IV. Phenyl derivatives of sepiolite and poly (organosiloxanes). *Colloid Polym. Sci.* **1992**, *270*, 165–176. [[CrossRef](#)]
82. Shimada, A.; Yoneyama, Y.; Tahara, S.; Mutin, H.; Sugahara, Y. Interlayer surface modification of the protonated ion-exchangeable layered perovskite  $\text{HLaNb}_2\text{O}_7\cdot x\text{H}_2\text{O}$  with organophosphonic acids. *Chem. Mater.* **2009**, *21*, 4155–4162. [[CrossRef](#)]
83. Machida, M.; Mitsuyama, T.; Ikeue, K.; Matsushima, S.; Arai, M. Photocatalytic property and electronic structure of triple-layered perovskite tantalates,  $\text{M}\text{Ca}_2\text{Ta}_3\text{O}_{10}$  (M = Cs, Na, H, and  $\text{C}_6\text{H}_{13}\text{NH}_3$ ). *J. Phys. Chem. B* **2005**, *109*, 7801–7806. [[CrossRef](#)]
84. Wang, Y.; Wang, C.; Wang, L.; Hao, Q.; Zhu, X.; Chen, X.; Tang, K. Preparation of interlayer surface tailored protonated double-layered perovskite  $\text{H}_2\text{Ca}_2\text{Ta}_3\text{O}_{10}$  with n-alcohols, and their photocatalytic activity. *RSC Adv.* **2014**, *4*, 4047–4054. [[CrossRef](#)]
85. Rodionov, I.A.; Maksimova, E.A.; Pozhidaev, A.Y.; Kurnosenko, S.A.; Silyukov, O.I.; Zvereva, I.A. Layered Titanate  $\text{H}_2\text{Nd}_2\text{Ti}_3\text{O}_{10}$  Intercalated With n-Butylamine: A New Highly Efficient Hybrid Photocatalyst for Hydrogen Production From Aqueous Solutions of Alcohols. *Front. Chem.* **2019**, *7*, 863. [[CrossRef](#)]
86. Voytovich, V.V.; Kurnosenko, S.A.; Silyukov, O.I.; Rodionov, I.A.; Minich, I.A.; Zvereva, I.A. Study of n-alkylamine Intercalated Layered Perovskite-Like Niobates  $\text{HCa}_2\text{Nb}_3\text{O}_{10}$  as Photocatalysts for Hydrogen Production From an Aqueous Solution of Methanol. *Front. Chem.* **2020**, *8*, 300. [[CrossRef](#)]
87. Fukuoka, H.; Isami, T.; Yamanaka, S. Crystal Structure of a Layered Perovskite Niobate  $\text{KCa}_2\text{Nb}_3\text{O}_{10}$ . *J. Solid State Chem.* **2000**, *151*, 40–45. [[CrossRef](#)]
88. Jehng, J.M.; Wachs, I.E. Structural Chemistry and Raman Spectra of Niobium Oxides. *Chem. Mater.* **1991**, *3*, 100–107. [[CrossRef](#)]
89. Kim, H.J.; Byeon, S.H.; Yun, H. Raman spectra of the solid-solution between  $\text{Rb}_2\text{La}_2\text{Ti}_3\text{O}_{10}$  and  $\text{RbCa}_2\text{Nb}_3\text{O}_{10}$ . *Bull. Korean Chem. Soc.* **2001**, *22*, 298–302.
90. Rodionov, I.A.; Sokolova, I.P.; Silyukov, O.I.; Burovikhina, A.A.; Fateev, S.A.; Zvereva, I.A. Protonation and Photocatalytic Activity of the  $\text{Rb}_2\text{La}_2\text{Ti}_3\text{O}_{10}$  Layered Oxide in the Reaction of Hydrogen Production. *Int. J. Photoenergy* **2017**, *2017*, 9628146. [[CrossRef](#)]